applied sciences

MDPI

Article

A Multi-Factor Comparative Study on H_2 and CO_2 Migration Behaviors in Saline Aquifers

Zihao Shi [1,2], Jiayu Qin [1,2,*], Nengxiong Xu [1,2,*], Yan Qin [1,2], Bin Zhang [1,2], Shuangxi Feng [3], Liuping Chen [4] and Hao Wang [4]

[1] School of Engineering and Technology, China University of Geosciences (Beijing), Xueyuan Road 29, Beijing 100083, China; zihaoshi@email.cugb.edu.cn (Z.S.); yanqin@cugb.edu.cn (Y.Q.); sc_zhb@cugb.edu.cn (B.Z.)
[2] Engineering and Technology Innovation Center for Risk Prevention and Control of Major Project Geosafety, MNR Ministry of Natural Resources of the People's Republic of China, Beijing 100083, China
[3] Department of Civil Engineering, Tianjin University, Tianjin 300354, China; shuangxi@tju.edu.cn
[4] China National Salt Industry Group Co., Ltd., Beijing 100055, China; jsb@chinasalt-jt.com (L.C.); ymxu@chinasalt-jt.com (H.W.)
* Correspondence: jiayu.qin@cugb.edu.cn (J.Q.); xunengxiong@cugb.edu.cn (N.X.)

Abstract

In contrast to CCUS/CCS, research on UHS in saline aquifers remains limited. Comparative analysis of H_2 and CO_2 migration offers a basis for transferring CCUS/CCS insights to UHS. Thus, to investigate how multiple factors affect H_2 and CO_2 migration in saline aquifers, this paper constructs various 3D models considering porosity, permeability, pressure, temperature, salinity, and capillary pressure. Numerical simulation results show that (1) H_2 exhibits strong fingering and wide plume spread, with low solubility and weak residual retention. CO_2 shows compact, stable plumes with high solubility and strong residual retention. (2) Low porosity enhances lateral migration and residual retention, especially for CO_2. (3) Reduced vertical permeability (K_v) significantly suppresses the upward migration of CO_2 and strengthens residual retention, whereas its effect on the H_2 migration range is less than 5%. Low horizontal permeability (K_h) mainly restricts lateral spreading and only slightly increases residual retention, but the sensitivity of H_2 is lower than that of CO_2. (4) Increased pressure promotes the dissolution of H_2 and CO_2. The dissolved amount of H_2 increased by approximately 16.15%, and CO_2 by about 7.49%. The temperature rise increases the solubility of H_2 and decreases that of CO_2. H_2 increased by approximately 15.56%, and CO_2 decreased by about 13.82%. The increase in salinity inhibited the dissolution of the two gases. H_2 and CO_2 decreased by approximately 17.5% and 16.6%, respectively. Additionally, high salinity weakens the temperature sensitivity of gas solubility. (5) Ignoring capillary pressure underestimates residual retention. However, it is mainly reflected in an increase in the retention scale and does not change the trend of residual retention controlled by different variables. These insights provide a basis for applying CCUS/CCS experiences to UHS.

Keywords: saline aquifers; CO_2 storage; H_2 storage; migration behaviors

check for updates

Academic Editor: Nikolaos Koukouzas

Received: 21 November 2025
Revised: 10 December 2025
Accepted: 11 December 2025
Published: 12 December 2025

Citation: Shi, Z.; Qin, J.; Xu, N.; Qin, Y.; Zhang, B.; Feng, S.; Chen, L.; Wang, H. A Multi-Factor Comparative Study on H_2 and CO_2 Migration Behaviors in Saline Aquifers. *Appl. Sci.* **2025**, *15*, 13107. https://doi.org/10.3390/app152413107

Copyright: © 2025 by the authors. Licensee MDPI, Basel, Switzerland. This article is an open access article distributed under the terms and conditions of the Creative Commons Attribution (CC BY) license (https://creativecommons.org/licenses/by/4.0/).

1. Introduction

Due to their wide distribution and favorable geological sealing conditions, underground saline aquifers provide an ideal geological environment for gas storage [1,2]. In terms of gas utilization, current research and practice primarily focus on carbon dioxide

(CO_2) capture, utilization, and storage (CCUS/CCS), as well as underground hydrogen (H_2) storage (UHS) [3]. Specifically, the research focus of CCUS/CCS is to capture CO_2 and inject it into saline aquifers [4,5]. As a potential solution for seasonal storage and a stable supply of H_2 energy, UHS has attracted widespread attention [6]. These gas storage technologies have become the key to the stable operation of future low-carbon energy systems.

Among these technologies, CCUS/CCS is the most extensively investigated [7,8]. In recent years, researchers have conducted comprehensive work from multiple situations [9,10]. Most studies integrate factors such as tectonic trapping conditions, reservoir physical properties, and CO_2–water interactions to analyze CO_2 migration and evaluate caprock integrity [11–13]. With continued advancements in numerical simulation, attention has increasingly shifted toward complex multi-field couplings, particularly the influence of thermo–hydro–mechanical–chemical (THMC) processes on CO_2 migration and storage performance [14–16]. In addition, the main mechanisms of CCUS/CCS include physical storage (structural and hydrodynamic trapping and residual retention), dissolution, and mineral solidification [17,18]. Consequently, numerous studies focus on these mechanisms [15,19–23]. For example, Mohamed and Ahmed demonstrated through numerical simulation the significant influence of mineral composition on the storage mechanism [22]. Jemal et al. extensively revealed long-term storage mechanisms such as dissolution and mineral solidification through numerical simulation. The results show that under the optimized conditions, dissolution and mineral solidification account for the vast majority of the sealed volume [23]. These in-depth studies provide support for the site selection evaluation of CCUS/CCS.

Similarly, many scholars have conducted numerous simulation studies on H_2 storage in saline aquifers [24]. For instance, injection and production cycles and rates [25,26], cushion gas volume and type [27,28], reservoir properties and environment [29], and well configuration [30]. Among these studies, Jadhawar and Saeed reported that the longer the storage period and the lower the injection and production frequencies, the greater the H2 storage capacity but the lower the recovery rate [26]. Zhao et al. focused on studying the influence of buffer gas types on UHS efficiency. The results showed that CO_2 as a buffer gas led to the highest purity of H_2 production, while CH_4 and N_2 as buffer gases had higher recovery rates and mobility [27]. Although some research work has been relatively complete, compared with CCUS/CCS, UHS is still in its infancy and requires further research.

The significant differences in physical and chemical properties between CO_2 and H_2 lead to their different migration behaviors in the saline aquifer [31]. In addition, the main purpose of CO_2 storage is to achieve long-term and stable sequestration [17]. H_2 storage in saline aquifers places more emphasis on H_2 storage efficiency and recyclability, and it is necessary to ensure the effective production and utilization of H_2 during peak energy demand periods [32]. Thus, to apply CCUS/CCS experiences to UHS, it is necessary to compare the migration behaviors of CO_2 and H_2 in saline aquifers under different influencing factors.

Comparative studies on H_2 and CO_2 systems remain scarce. Existing modeling in saline aquifers has mainly focused on how injection strategies and operational factors affect storage performance. Bai et al. [31] showed that H_2 storage efficiency is more sensitive to heterogeneity and injection strategy than CO_2, while Misaghi et al. [33] found that H_2 plumes rely mainly on structural trapping, whereas CO_2 increasingly benefits from dissolution and residual trapping. However, there are no reports on the systematic comparison of the migration behaviors of H_2 and CO_2 under the influence of reservoir properties and reservoir environment.

This paper conducts a comparative study on the migration behaviors of H_2 and CO_2 under different influencing factors through numerical simulation methods. The study mainly focuses on key reservoir parameters (porosity and permeability) and reservoir environment (pressure, temperature, and salinity). Considering that capillary pressure depends on porosity and permeability, it has an impact on residual gas retention. Thus, this article supplements the influence of capillary pressure. Ultimately, the migration behaviors of H_2 and CO_2 in saline aquifers under different influencing factors are compared. The research results provide theoretical support for leveraging CCUS/CCS experience in UHS.

The rest of this study is organized as follows: Section 2 provides a comparative analysis of H_2 and CO_2, including their fundamental physicochemical properties and the differences in storage mechanisms, and further introduces the theory of relative permeability and hysteresis effects. Section 3 presents the computational models and research design, mainly including parameter selection, model construction, and the establishment of comparison schemes. Section 4 analyzes the simulation results. Section 5 is the discussion. Finally, Section 6 summarizes the conclusions, identifies the limitations, and outlines directions for future work.

2. Background

2.1. Comparison of H_2 and CO_2

Due to the substantial differences in the physical and chemical properties of H_2 and CO_2, their distribution, trapping behaviors, and evolution mechanisms in saline aquifers also differ fundamentally. Thus, it is first necessary to clarify the physicochemical properties and storage objectives of CO_2 and H_2, identify the similarities and differences between their trapping mechanisms, and provide a theoretical foundation for subsequent numerical simulations.

Table 1 summarizes the key physicochemical properties of the two gases [34]. Notably, the molecular weight of H_2 is only 2.016 g/mol, compared with 44.009 g/mol for CO_2. As a result, the density of H_2 is far lower than that of CO_2, leading to higher mobility. In contrast, the higher density of CO_2 enables it to form more stable accumulations. With respect to phase characteristics, the critical temperature of H_2 is only 33.2 K, whereas that of CO_2 is 304.21 K. Under typical reservoir temperature and pressure conditions, CO_2 exists predominantly as a supercritical fluid, while H_2 remains in the gaseous phase. Accordingly, H_2 exhibits higher compressibility and a more sensitive pressure response, whereas CO_2 demonstrates greater volumetric stability. In terms of flow and migration behavior, H_2 has low viscosity, a high migration coefficient, and rapid seepage rates, resulting in a greater potential for migration and leakage. In contrast, the relatively higher viscosity and slower migration rate of CO_2 contribute to more stable storage. In addition, the solubility of CO_2 in water is much higher than that of H_2, making CO_2 more susceptible to dissolution and mineral solidification.

During gas storage in saline aquifers, the storage of injected fluids occurs primarily through structural and hydrodynamic trapping, residual retention, dissolution, and mineral solidification [17]. Structural and hydrodynamic trapping are the most fundamental storage mechanisms: the former relies on impermeable caprock structures (such as anticlines), whereas the latter is formed by the lateral hydraulic gradient. These two mechanisms are largely independent of gas type and dominate short-term storage behavior. Residual retention arises from isolated gas ganglia immobilized within the aqueous phase. Because H_2–water interfacial tension is high, the residual saturation of H_2 is generally lower than that of CO_2, and CO_2 is more likely to form stable trapped gas clusters due to wettability alteration. Dissolution is governed by gas solubility in formation water. CO_2 exhibits strong solubility, whereas H_2 is only sparingly soluble. Mineral solidification is relevant

primarily for CO_2, which can react with formation minerals to produce carbonates and achieve long-term geochemical sequestration.

Table 1. Comparison of the physicochemical properties of CO_2 and H_2 in standard conditions [34].

Parameter	H_2	CO_2	Unit
Molecular weight	2.016	44.009	g/mol
Density	0.08375	1.842	kg/m^3
Dynamic viscosity	0.892	1.493	$\times 10^{-5}$ Pa·s
Specific gravity	0.07	1.52	-
Boiling point	20.28	194.65	K
Critical temperature	33.19	304.21	K
Critical pressure	1.31	7.38	MPa
Critical density	31.43	468.19	kg/m^3
Solubility in pure water	0.00016	0.169	g/100 g H_2O
Diffusion coefficient in air	0.756	0.16	cm^2/s
Heating value	120–141.7	-	kJ/g
Interfacial tensions (IFT)	65–72	20–35	mN/m
Chemical characteristics	Exhibits strong reducing properties and readily reacts with oxidizing agents	Acidic oxide reacts with bases and other oxidation–reduction processes.	-

Note: The IFT between H_2 and CO_2 is within the range of values under reservoir conditions.

Overall, H_2 storage relies mainly on structural and hydrodynamic trapping, while other mechanisms reduce its recoverable fraction. In contrast, CO_2 sequestration benefits significantly from residual, dissolution, and mineral solidification. Figure 1 illustrates the temporal evolution of these trapping mechanisms [35].

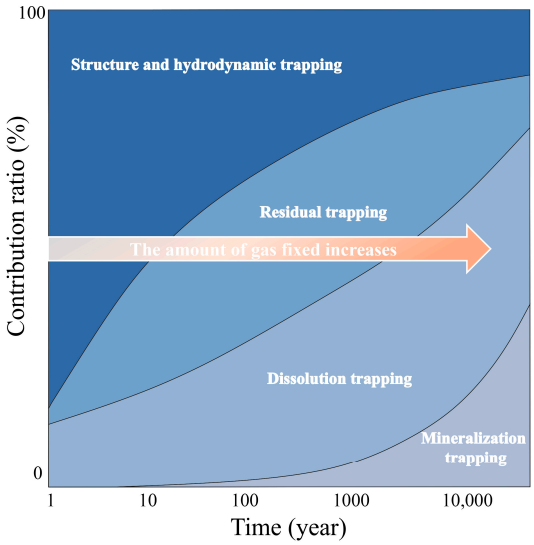


Figure 1. Temporal evolution of different storage mechanisms (revised from Ref. [35]).

2.2. Multiphase Flow Theoretical Method

Before conducting numerical simulation calculations, it is necessary to clarify the theoretical method for the heterogeneous flow behavior generated after the injection of CO_2 and H_2 into the saline aquifer. It mainly includes the state equation describing the multiphase flow theory, the gas-water relative permeability and its hysteresis effect, capillary pressure, and the dissolution behavior of gases.

For gas-water systems, especially CO_2-water systems, the Peng-Robinson equation of state (PR-EOS) with appropriate binary interaction parameters (BIPS) performs well in terms of gas capture and mutual solubility. Thus, this paper adopts PR-EOS [36]. Due to the limited availability of capillary pressure data for H_2, and given that capillary pressure is

in direct proportion to interfacial tension when all other conditions remain unchanged [37], we estimate the capillary pressure curve for H_2 by scaling the CO_2 curve using the ratio of their interfacial tensions (2.3 times that of CO_2). In this paper, the interfacial tensions of H_2 and CO_2 are taken as 30 mN/m and 69 mN/m, respectively. The capillary pressure curve is shown in Figure 2. The rock fracture pressure is determined based on the forward formation rock fracture pressure gradient of 0.0182–0.0190 MPa/m [38].

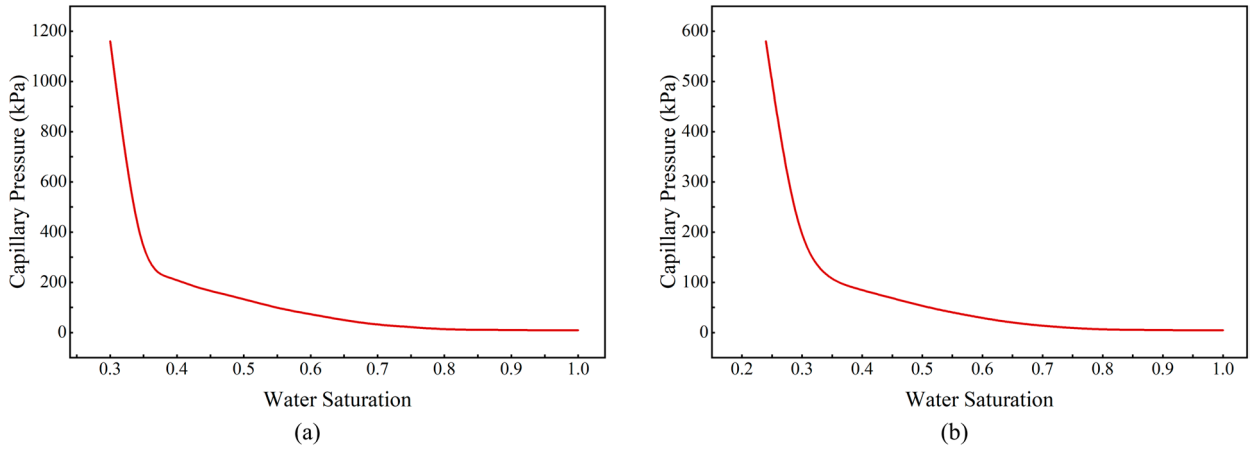


Figure 2. Capillary pressure curve: (**a**) H_2, (**b**) CO_2.

In this paper, the relative permeability of gas and water is described according to the power-law relationship in the generalized Corey model [39]:

$$k_{ri} = k_{ri,max}\left(\frac{S_i - S_{ir}}{1 - \sum_i S_{ir}}\right)^{n_i} \quad (1)$$

where k_{ri} is the relative permeability of phase i, $k_{ri,max}$ is the ultimate relative permeability of phase i, S_i is the saturation of phase i, S_{ir} is the residual saturation of phase i, and n_i is the Corey index of phase i. The gas-water relative permeability curve is shown in Figure 3.

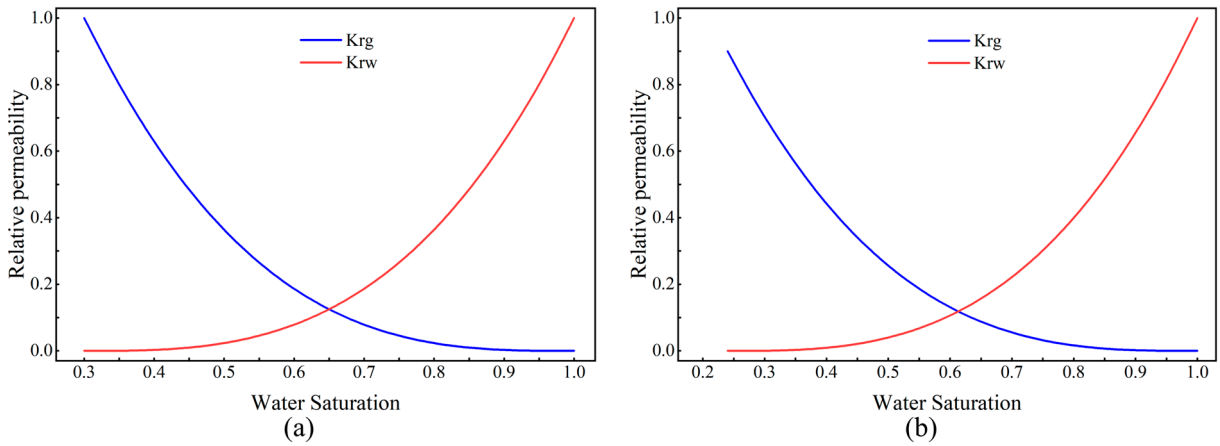


Figure 3. The relative permeabilities of gas and water: (**a**) H_2, (**b**) CO_2.

The relative permeability hysteresis effect refers to the phenomenon that, during the water reverse gas displacement process, the wetting phase is more likely to fill the pores,

resulting in the non-wetting phase being trapped in the pores. In this paper, the linear Land model is introduced to calculate the phase seepage hysteresis phenomenon [40]:

$$S_{gr}^{*} = \frac{S_{gi}}{1 + CS_{gi}} \tag{2}$$

$$C = \frac{1}{S_{gi,\,max}} - 1 \tag{3}$$

where S_{gr}^{*} is the capture gas saturation, S_{gi} is the initial water saturation, and C is the Land constant.

Initial formation water is in a saturated state, and the solubility of gas in water is calculated by using Henry's Law corrected for pressure and temperature [41–43].

$$ln(f/b) = lnH_i + \left[V\left(p - p_{ref}\right)/RT\right] \tag{4}$$

where f is the gas fugacity, b is the mole fraction of gas in water, H_i is Henry's law constant, V is the partial molar volume of gas at infinite dilution, R is the universal gas constant, T is the temperature, p is the pressure, and p_{ref} is the reference pressure.

The above Henry constant is based on the function of temperature and pressure under pure water. Under reservoir conditions, the modified Henry constant affected by salinity is calculated by the following equation [44,45].

$$\log_{10}\left(\frac{H_{salt,i}}{H_i}\right) = k_{salt,i}m_{salt} \tag{5}$$

where $H_{salt,\,i}$ is Henry's constant of component i in brine (salt solution), $k_{salt,\,i}$ is the salting-out coefficient for component i, and m_{salt} is the molality of the dissolved salt (mol/kg H_2O).

3. Computational Model and Simulation Design

This paper mainly examines the differences in the migration behaviors of H_2 and CO_2 in saline aquifers under reservoir properties and gas-water interaction. Thus, a simplified 3D model is adopted for calculation. All parameter Settings are within the general parameter range of the saline aquifer [46–48].

3.1. Computational Model

The simulation is performed using a 3D geological model of a cubic aquifer with dimensions of 1000 m in length, 1000 m in width, and 60 m in height, with a burial depth of 1690 m. The mesh size is set at 10 m in the horizontal direction and 4 m in the vertical direction, discretizing the aquifer into 15,000 grid blocks. The model closes boundaries at the top and bottom to simulate an impermeable caprock. The infinite extent of the saline aquifer is simulated by multiplying the pore volume of the lateral boundary mesh by 1000. Thus, during the UHS and CCUS/CCS processes, water can freely enter and exit from the boundary, and this method will also effectively reduce the abnormal pressure accumulation effect of the model. At first, the aquifer is completely saturated with water, and there is no gas present. The static water pressure determines the initial pressure distribution, and the pressure at the top of the model is 17,500 kPa. All reservoir parameters in the calculation model presented in this paper are calculated using the mean value. The porosity of the basic model is 0.1, the horizontal and vertical permeabilities are 50 mD, and the reservoir temperature is 55 °C. The porosity and permeability conditions set by the basic model represent moderately permeable saline aquifers, which are widely distributed in reality. The basic calculation models are divided into CO_2 injection models and H_2 injection models.

Except for the differences caused by gas properties (except for the capillary pressure curve), all other settings remain consistent. The basic calculation model is shown in Figure 4, and the calculation parameters are presented in Table 2.

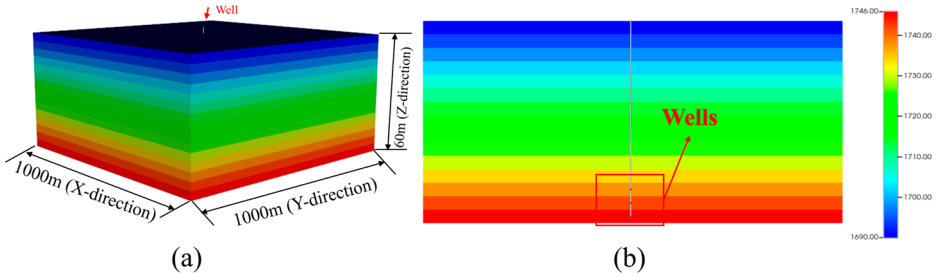


Figure 4. The basic calculation model: (**a**) 3D view, (**b**) XY view.

Table 2. Calculation parameters of the basic model.

Parameter	Value	Unit
Number of grid	150,000	-
Grid dimension X × Y × Z	10 × 10 × 15	m
Reference depth	1690	m
Reference pressure	17,500	kPa
Temperature	55	°C
Porosity	10	%
Permeability	50	mD
Rock compressibility	5×10^{-9}	kPa^{-1}
Initial water saturation	100	%
Water salinity	0	mol/kg

3.2. Simulation Design

In this paper, the multi-component simulator CMG-GEM™ 2022.1 is used to conduct a comparative study on the migration behaviors of UHS and CCUS/CCS in saline aquifers through numerical simulation methods. CMG-GEM™ can simultaneously calculate several storage mechanisms existing in saline aquifers. Multiple simulation schemes alter the porosity of the reservoir, permeability, temperature, pressure, and salinity. Meanwhile, the degrees to which the basic model, porosity model, and permeability model are affected by capillary pressure are compared. Exploring the effects of these factors on the structure and hydrodynamic trapping of CO_2 and H_2, residual retention, and dissolution.

Before the simulation, the engineering operation parameters of the computing model need to be set. Settings are as follows:

(1) Vertical well perforation is carried out in the middle of the calculation model, and perforation gas injection is performed at three grids in the vertical direction at the bottom of the reservoir.
(2) To avoid the influence of cushion gas mixing, no cushion gas injection is set up in this paper.
(3) This paper does not conduct short-term gas circulation injection and production operations. The calculation model injects gas at a rate of 30,000 m^3/day at three perforations at the bottom of the reservoir for one year.
(4) This paper conducts a comparative study on the time scale of H_2, that is, the two gases are injected at the bottom of the saline aquifer for one year and then migrate for one year after the injection stops.
(5) The minimum fracture pressure of the rock is determined as 31,444 kPa based on the forward formation rock fracture pressure gradient of 0.0188 MPa/m. The maximum

bottom hole pressure (BHP) was limited to no more than 90% of the minimum fracture pressure of the rock, and the final determination of BHP was 28,300 kPa.

The gas injection well is located at the center of the model, 500 m away from the boundary grid. Thus, the material flow around the wellbore is not affected by the boundary. Except for porosity, permeability, temperature, pressure, salinity, and capillary pressure, other attributes remain consistent with the basic model. The comparison plan is as follows:

(1) This paper systematically investigates the influence of porosity on the migration behavior of UHS and CCUS/CCS in saline aquifers. The porosity of the comparison models is 0.05, 0.15, 0.2, and 0.25, respectively.
(2) Due to the anisotropy of permeability, the influence of horizontal permeability (K_h) and vertical permeability (K_v) is investigated, respectively, in this paper. The penetration rates of the comparison models are 5 mD, 15 mD, 25 mD, and 35 mD, respectively.
(3) The temperature comparison models are, respectively, set at 65 °C, 75 °C, 85 °C, and 105 °C.
(4) The pressure comparison models are, respectively, set at 16,500 kPa, 18,500 kPa, 19,500 kPa, and 21,500 kPa.
(5) In the basic model, the water is pure (with a mineralization degree of 0 g/L). In the salinity comparison model, the mineralization degree of water is changed in units of molar mass concentration, and it is classified into brackish water, saline water, highly saline water, and high brine. The mineralization composition of water in all models is set to NaCl. The salinities of the comparison models are 0.051 mol/kg, 0.171 mol/kg, 0.873 mol/kg, and 6 mol/kg, respectively.
(6) Considering that temperature changes can affect the salting-out effect, this paper also investigated the behavioral differences of CO_2 and H_2 at five salinity levels (0 mol/kg, 0.171 mol/kg, and 0.873 mol/kg) under the influence of five temperatures (55 °C, 65 °C, 75 °C, 85 °C, and 105 °C).
(7) To explore the influence of capillary pressure, capillary pressure curves are set for the basic model, two porosity comparison models (0.15 and 0.25), and two permeability comparison models (5 mD and 15 mD), and the migration law of gas in the saline aquifer with and without capillary action is studied.

As the simulation period is two years, this paper does not consider biochemical mineral reactions that have a significant impact on long-term capture. The calculation scheme is shown in Table 3.

Table 3. Numerical simulation scheme.

Model	Comparison Scheme	Unit
Base	Capillary pressure is not considered.	-
Porosity	0.05, 0.15, 0.2, and 0.25	%
Permeability	Horizontal permeability: 5, 15, 25, and 35 Vertical permeability: 5, 15, 25, and 35	mD
Pressure	16,500, 18,500, 19,500, and 21,500	kPa
Temperature	65, 75, 85, and 105	°C
Salinity	0.051, 0.171, 0.873, and 6	mol/kg
Capillary Pressure	Incorporated into the base case, porosity scenarios, and permeability scenarios	-

4. Results and Analysis

This paper compares the effects of different factors, such as porosity, permeability, temperature, pressure, salinity, and capillary pressure, on the migration range, residual retention amount, and maximum dissolution amount of H_2 and CO_2 in the saline aquifers after two years. Specifically, porosity, permeability, and capillary models focus on the

migration and residual retention behaviors of gases. The temperature, pressure, and salinity models mainly assess the maximum dissolution amount of gases. The dissolution parameters are mainly the maximum molar fraction of gases in water, while the mass molar concentration of gases is added for reference. In addition, in order to express the rule more intuitively, the corresponding parameters are used to represent the base case when performing comparative analysis.

4.1. Basic Case

In the basic case, the porosity is 0.1, both K_v and K_h are 50 mD, the pressure is 17,500 kPa, the constant temperature is 55 °C, the mineralization degree of water is 0 mol/kg, and the capillary pressure is not considered.

Figure 5 illustrates the gas saturation distributions of H_2 and CO_2. Owing to its low density, low viscosity, and strong buoyancy, H_2 forms a sharp, vertically elongated plume with significant lateral spreading. In contrast, CO_2, in its supercritical state with higher density and viscosity, develops thicker, more stable plumes with shorter migration distances. Differences in solubility further influence migration: under baseline conditions, H_2 reaches a maximum mass fraction of 0.002228 and a molar concentration of 0.1267 mol/kg, whereas CO_2 attains 0.0217 and 1.23 mol/kg, respectively.

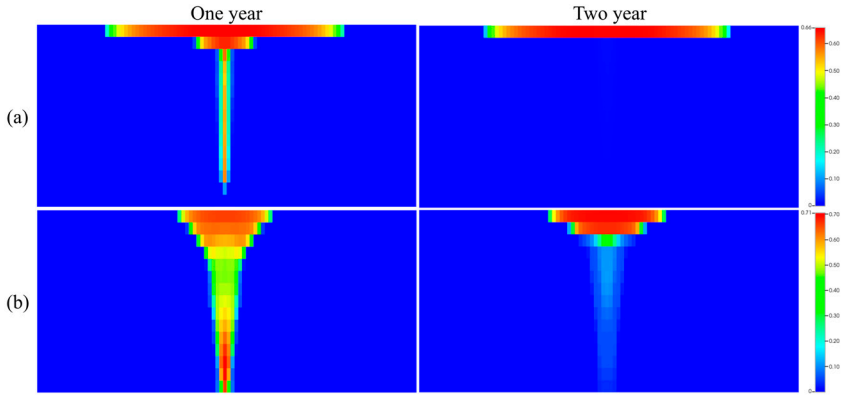


Figure 5. Gas saturation of H_2 and CO_2: (**a**) H_2, (**b**) CO_2.

Figure 6 further illustrates the residual gas saturation of H_2 and CO_2. As shown in Figure 6a, H_2 exhibits relatively low residual saturation, forming only localized retention zones. In contrast, Figure 6b shows that CO_2 has higher residual saturation with a broader distribution. This difference primarily arises from the lower interfacial tension of the CO_2–water system, which facilitates the formation of disconnected gas clusters. Conversely, H_2's higher interfacial tension promotes reconnection and continued migration, resulting in weaker residual.

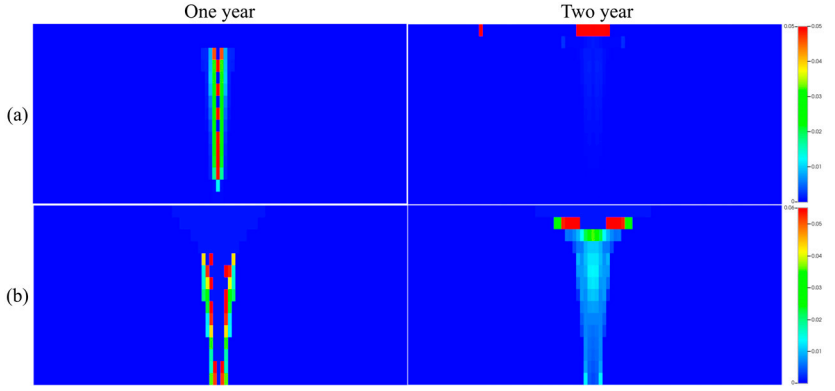


Figure 6. Residual saturation of H_2 and CO_2: (**a**) H_2, (**b**) CO_2.

4.2. Effect of Porosity

Figure 7 illustrates the effect of porosity on gas migration. As porosity decreases, gas accumulation near the reservoir top becomes noticeably weaker, while the overall migration range expands. The main reason is that the decrease in porosity narrows the pore throat, increases the tortuosity, and reduces the flow cross-sectional area, thereby increasing the flow resistance and promoting lateral diffusion. For H_2, the residual saturation reaches 0.35 at a migration distance of 200 m when porosity is 0.25, but remains as high as 0.38 even at 420 m when porosity decreases to 0.05—an increase in migration distance of more than 110%. CO_2 exhibits a similar trend: its saturation rises from 0.37 at 80 m to 0.53 at 210 m under the same porosity reduction, corresponding to an expansion in migration range exceeding 160%.

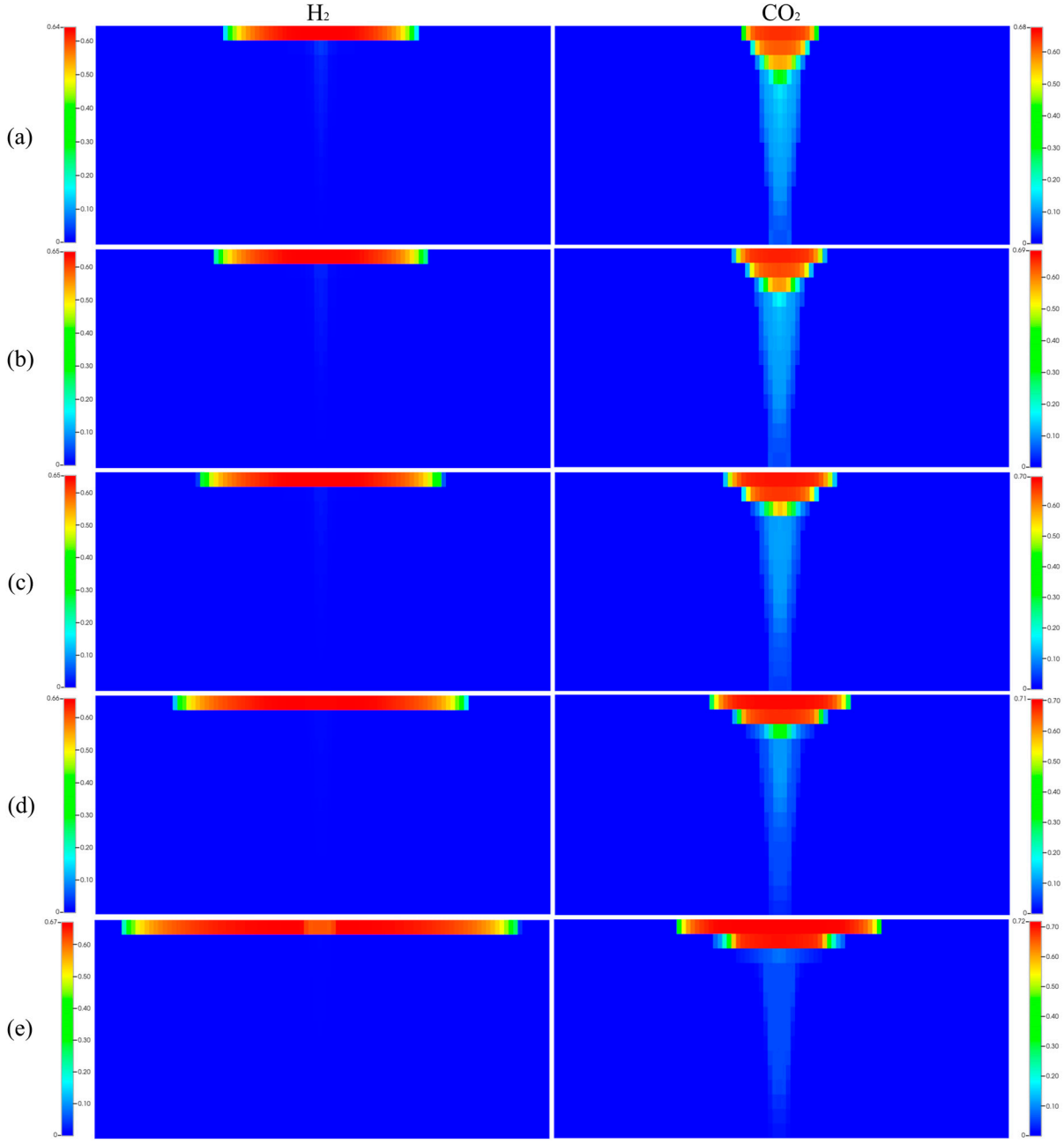


Figure 7. Saturation of two gases at different porosities: (**a**) 0.25, (**b**) 0.2, (**c**) 0.15, (**d**) 0.1, (**e**) 0.05.

Figure 8 illustrates the effect of porosity on residual gas retention in the saline aquifer. As porosity decreases, residual gas saturation near the reservoir top increases, while retention of upward-migrating gas gradually weakens. During lateral migration, H_2 residuals become more dispersed and exhibit a broader spatial spread, whereas CO_2 shows a more pronounced vertical stacking of residual saturation, forming clearer stratified enrichment zones. As shown in Figure 8a,e, increasing porosity reduces the maximum H_2 residual saturation from 0.05 to 0.015, while CO_2 maintains an almost unchanged peak value across the same porosity range. Accordingly, when porosity increases from 0.05 to 0.25, the difference in maximum residual saturation between CO_2 and H_2 expands from 16.7% to 77.8%, accompanied by a noticeable broadening of the spatial contrast in their respective residual retention.

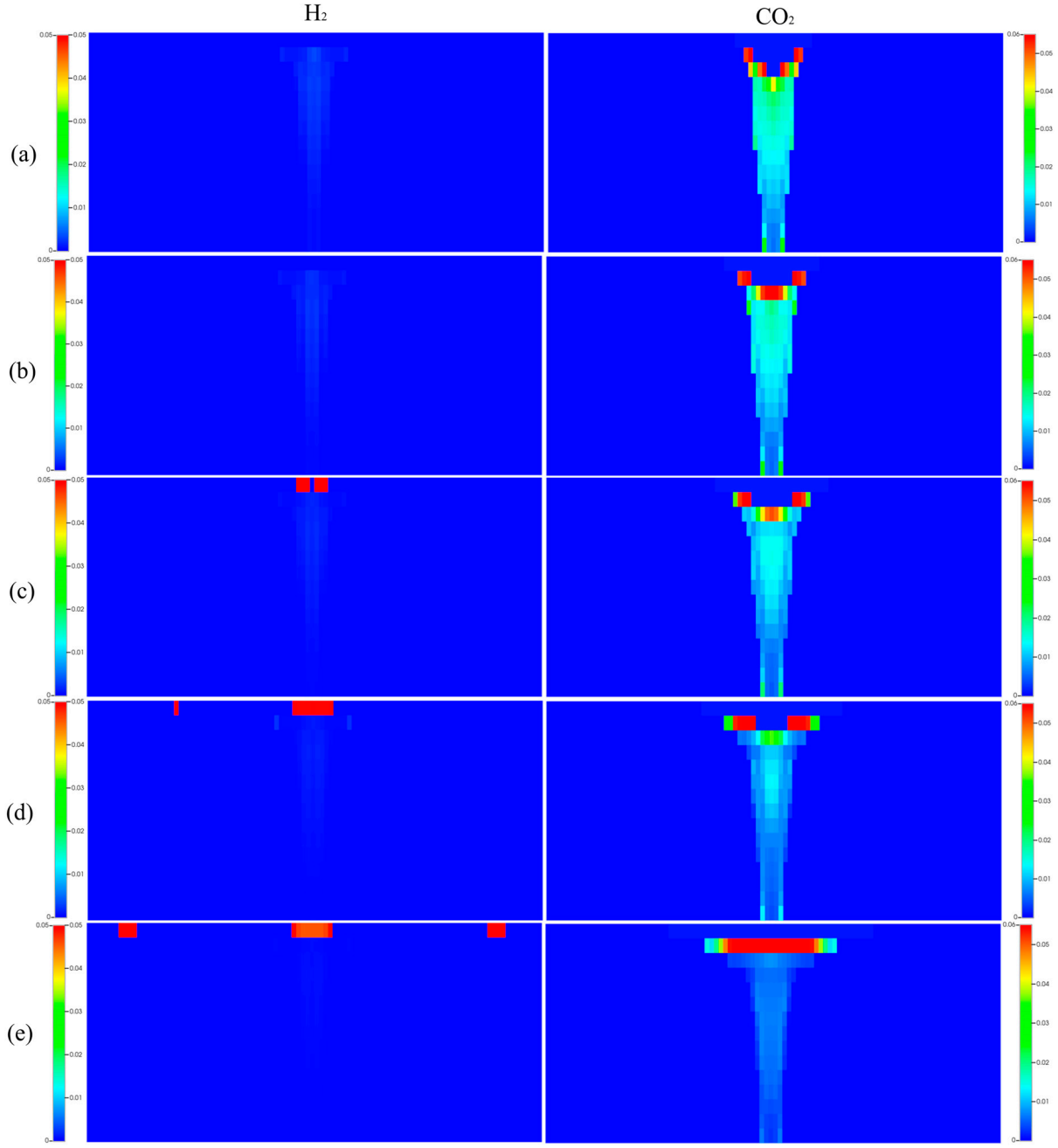


Figure 8. Residual saturation of two gases under different porosities: (**a**) 0.25, (**b**) 0.2, (**c**) 0.15, (**d**) 0.1, (**e**) 0.05.

4.3. Effect of Permeability

Figure 9 shows that reducing K_v constrains the plume extent of both gases, but the degree of sensitivity differs markedly. The H_2 plume consistently exhibits a highly elongated fingering morphology dominated by buoyancy, and variations in K_v have only a minor effect, with the change in maximum migration distance remaining within 5%. In contrast, CO_2 is significantly more sensitive to K_v. Under low K_v conditions, pronounced vertical stratification and near-wellbore accumulation occur, and this layering effect weakens as K_v increases. When K_v is 5 mD, the peak local saturation of CO_2 reaches 0.66, whereas under higher K_v it drops to around 0.10, representing an 84.9% reduction.

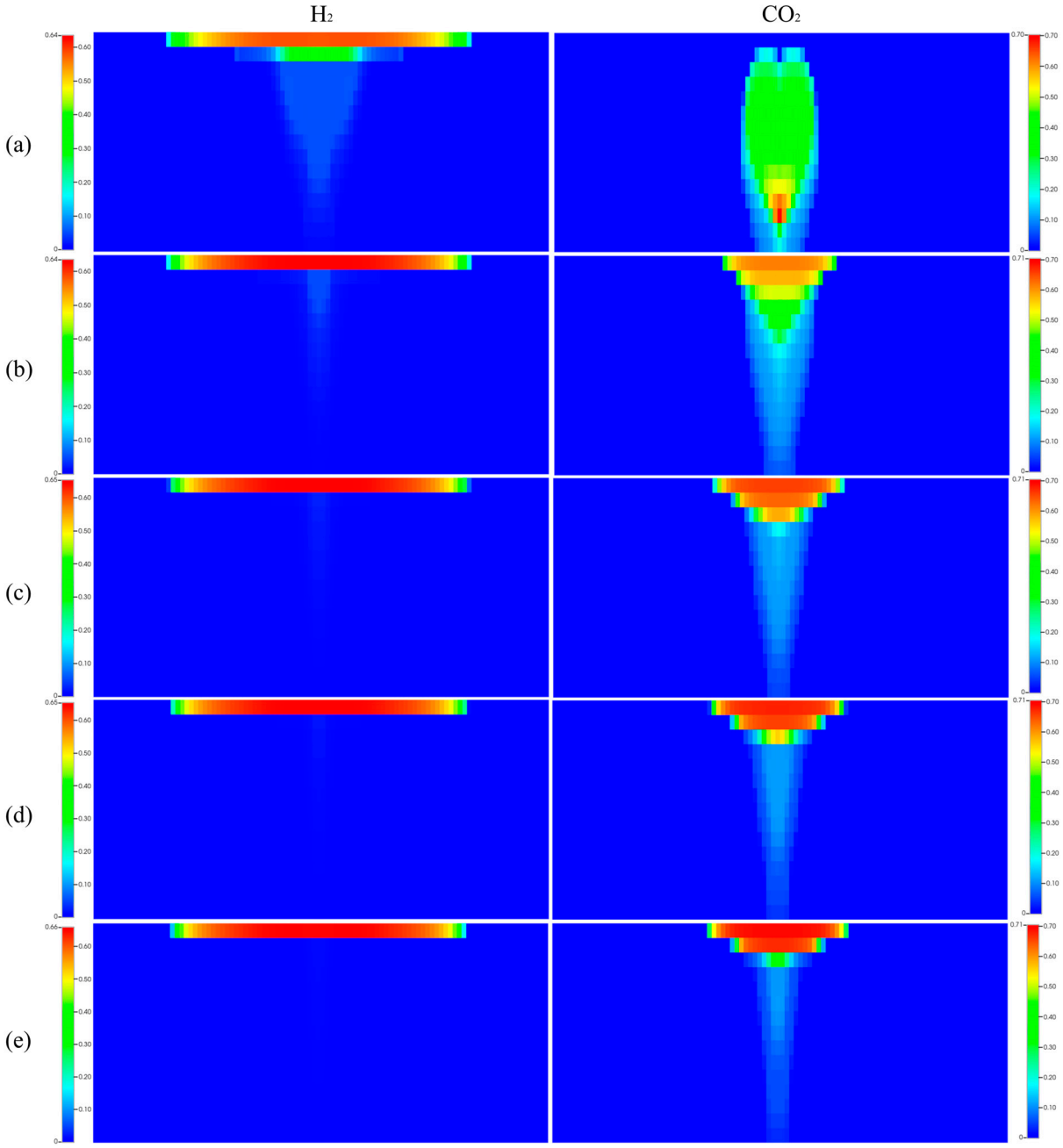


Figure 9. Saturation of two gases at different K_v: (**a**) 5 mD, (**b**) 15 mD, (**c**) 25 mD, (**d**) 35 mD, (**e**) 50 mD.

Figure 10 illustrates the effect of K_v on residual retention. As K_v decreases, the residual enrichment zones of both gases shift downward, but their spatial distributions differ notably. Under high K_v, H_2 forms only a localized residual accumulation near the top boundary. As

K_v declines, its residual saturation progressively migrates downward, with a relatively low maximum value (0.036) but a considerably larger lateral spread. In contrast, CO_2, owing to its greater density, higher aqueous solubility, and stronger trapping, more readily forms vertically stratified residual retention. This stratification becomes increasingly pronounced under low K_v, where reduced vertical connectivity enhances CO_2's tendency to accumulate in discrete layers, leading to a clearer separation between upper free fluid flow zones and lower residual zones.

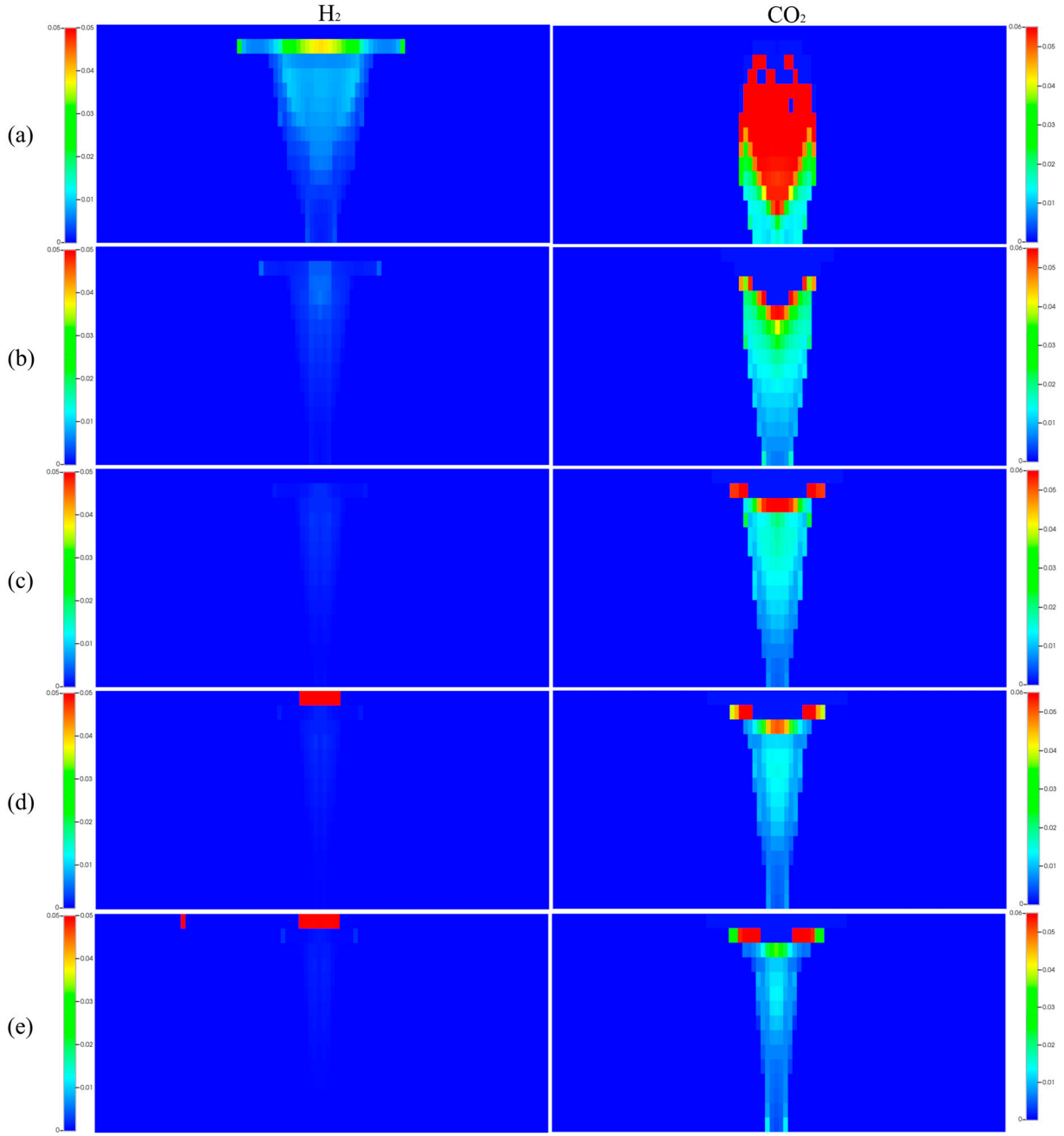


Figure 10. Residual saturation of two gases at different K_v: (**a**) 5 mD, (**b**) 15 mD, (**c**) 25 mD, (**d**) 35 mD, (**e**) 50 mD.

Figure 11 demonstrates that the influence of K_h on gas migration differs fundamentally from the effect of K_v. As K_h decreases, the lateral transmissibility of the reservoir weakens, causing the horizontal extent of the plume to contract. Under low K_h conditions, CO_2 develops a typical inverted-cone enrichment pattern that concentrates around the injection

well—markedly different from the vertical layering observed under low K_v. For example, under low K_h, the CO_2 saturation near the top can reach 0.67, whereas under low K_v, the saturation at the top approaches zero. Although H_2 is less sensitive to K_h variations than CO_2, K_h still imposes a more pronounced restriction on H_2 migration compared with K_v. As K_h decreases, H_2 fingering weakens, and its maximum lateral migration distance decreases from about 330 m at K_h = 50 mD to 280 m at 5 mD, representing a 15% reduction.

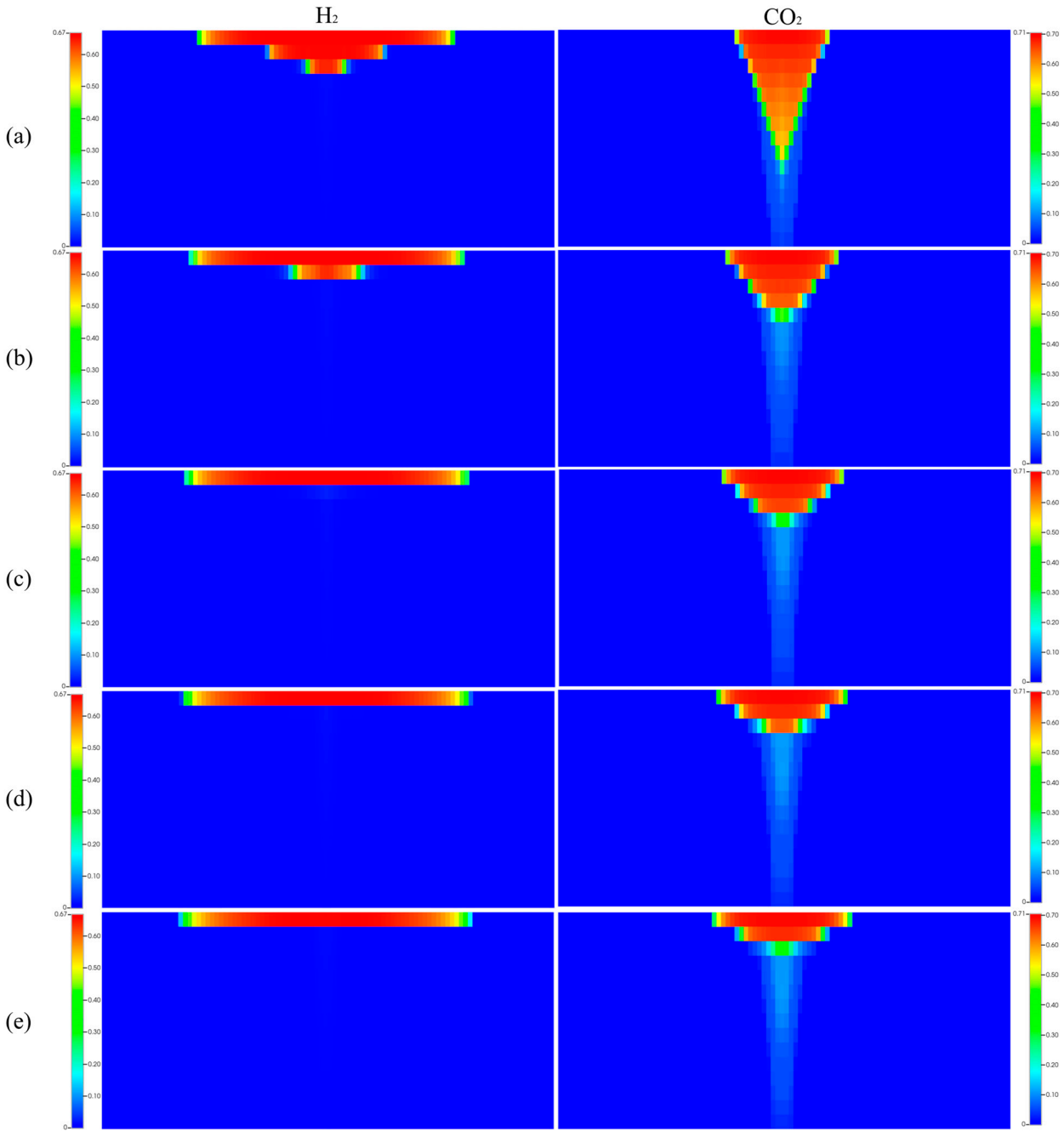


Figure 11. Saturation of two gases at different K_h: (**a**) 5 mD, (**b**) 15 mD, (**c**) 25 mD, (**d**) 35 mD, (**e**) 50 mD.

Figure 12 demonstrates that the impact of K_h on residual gas retention remains comparatively limited. For both H_2 and CO_2, the behavioral trends exhibit pronounced consistency, implying that horizontal permeability does not serve as the primary control on variations in residual retention characteristics. Although changes in K_h lead to a vertical repositioning of the enrichment zone, the areal extent of the residual-retention region and the peak

local residual saturation show minimal variation. These results collectively indicate that reductions in K_h mainly rearrange the spatial distribution of residual retention rather than substantially influencing the overall magnitude of residual saturation.

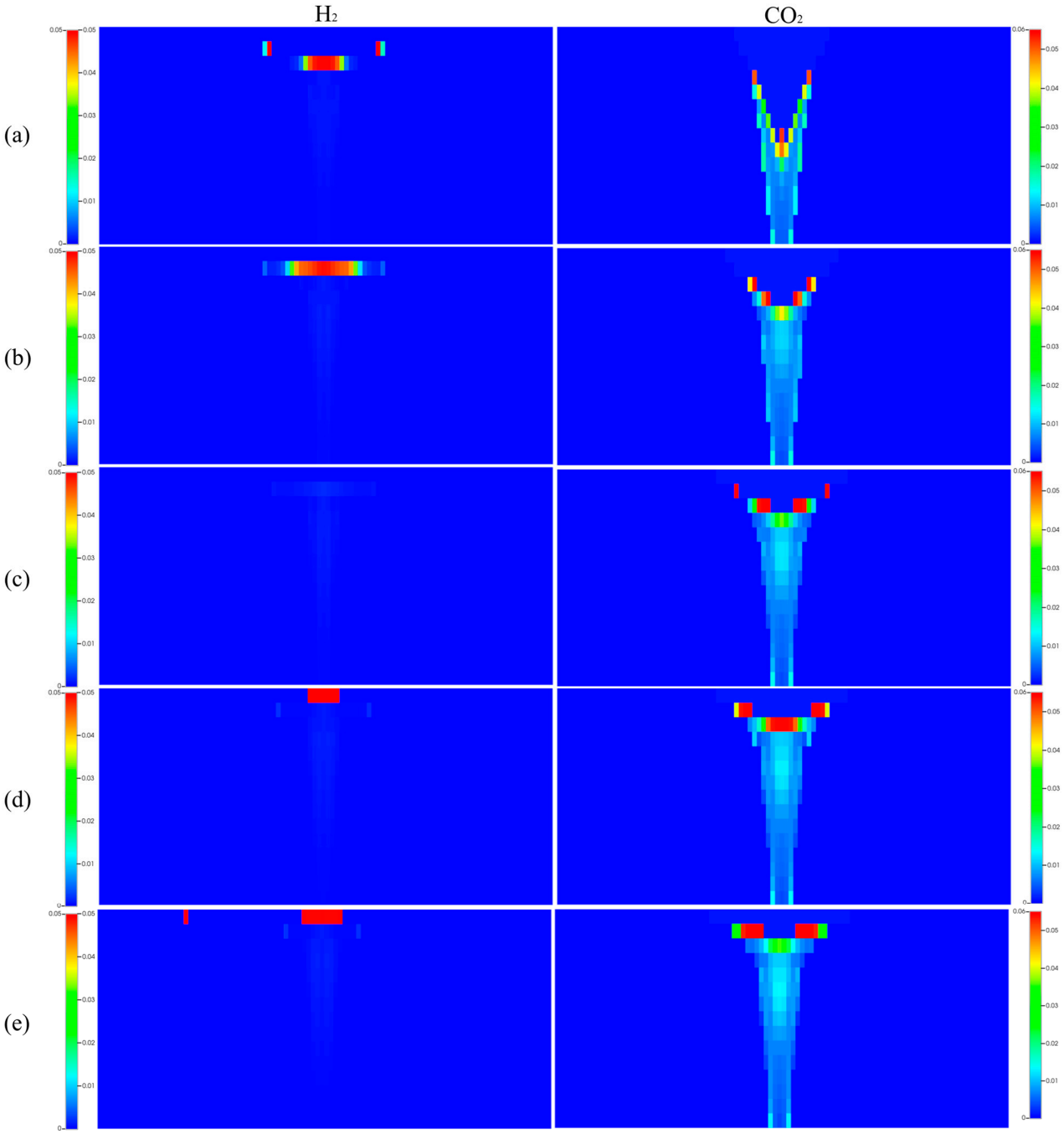


Figure 12. Residual saturation of two gases at different K_h: (**a**) 5mD, (**b**) 15 mD, (**c**) 25 mD, (**d**) 35 mD, (**e**) 50 mD.

4.4. Effect of Pressure, Temperature, and Salinity

Figure 13 presents the impact of pressure on gas solubility. With increasing pressure, the maximum dissolution amounts of both gases rise. However, H_2 is more pressure-sensitive than CO_2. When pressure increases from 16,500 kPa to 21,500 kPa, the mole fraction of dissolved H_2 increases from 0.00218 to 0.00260, representing a 16.15% growth. Under the same pressure change, the mole fraction of CO_2 increases from 0.021 to 0.0227, an increase of only 7.49%.

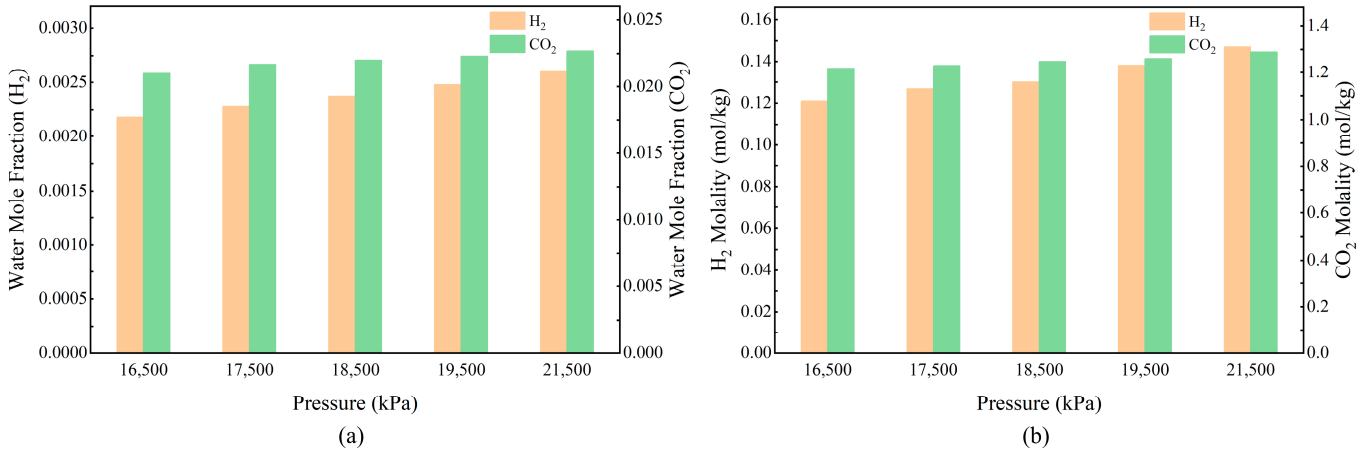


Figure 13. Dissolution changes of H_2 and CO_2 at different pressures: (**a**) The molar fraction of a gas in water; (**b**) the mass molar concentration of a gas.

Figure 14 shows the influence of temperature on gas solubility. Unlike the pressure effect, rising temperature enhances the solubility of H_2 while suppressing that of CO_2. As the temperature increases from 55 °C to 105 °C, the mole fraction of dissolved H_2 increases from 0.00228 to 0.00270, a rise of approximately 15.56%. Conversely, the dissolved mole fraction of CO_2 decreases from 0.027 to 0.0187, a reduction of 13.82%.

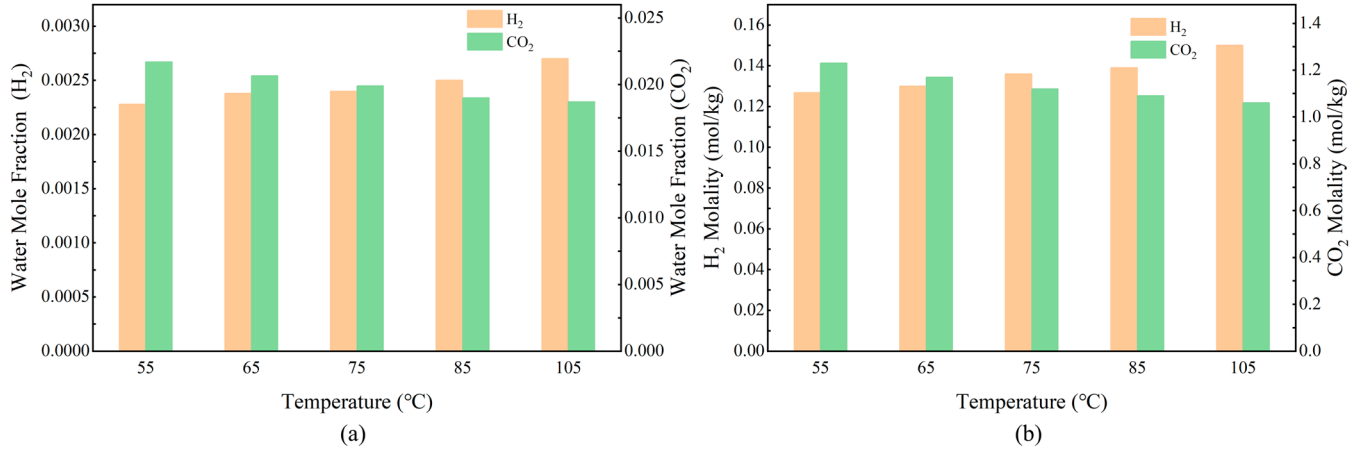


Figure 14. Dissolution changes of H_2 and CO_2 at different temperatures: (**a**) The molar fraction of a gas in water; (**b**) the mass molar concentration of a gas.

Figure 15 illustrates the effect of salinity on gas solubility. As salinity increases, the maximum dissolution amounts of both gases decrease, and the difference in their sensitivity to salinity is relatively minor. When salinity rises from 0 mol/kg to 0.873 mol/kg, the dissolved mole fraction of H_2 decreases from 0.00228 to 0.00188—a 17.5% reduction. CO_2 decreases from 0.0217 to 0.0181, a 16.6% reduction, slightly lower than that of H_2. Under extremely high mineralization (6 mol/kg), gas solubility sharply decreases, with H_2 decreasing by more than 75% and CO_2 by over 70%.

Figure 16 shows that gas solubility exhibits the same temperature-dependent trend across different salinities, but higher salinity weakens the sensitivity of dissolution to temperature. This effect is stronger for H_2 than for CO_2. As the temperature rises from 55 °C to 105 °C, H_2 solubility increases by about 15.56% in pure water but only 14.5% in highly saline water, representing a 1.06% reduction in sensitivity. CO_2 solubility decreases by 13.82% in pure water and 13.2% in saline water, reducing its temperature-dependent decline by roughly 0.6%.

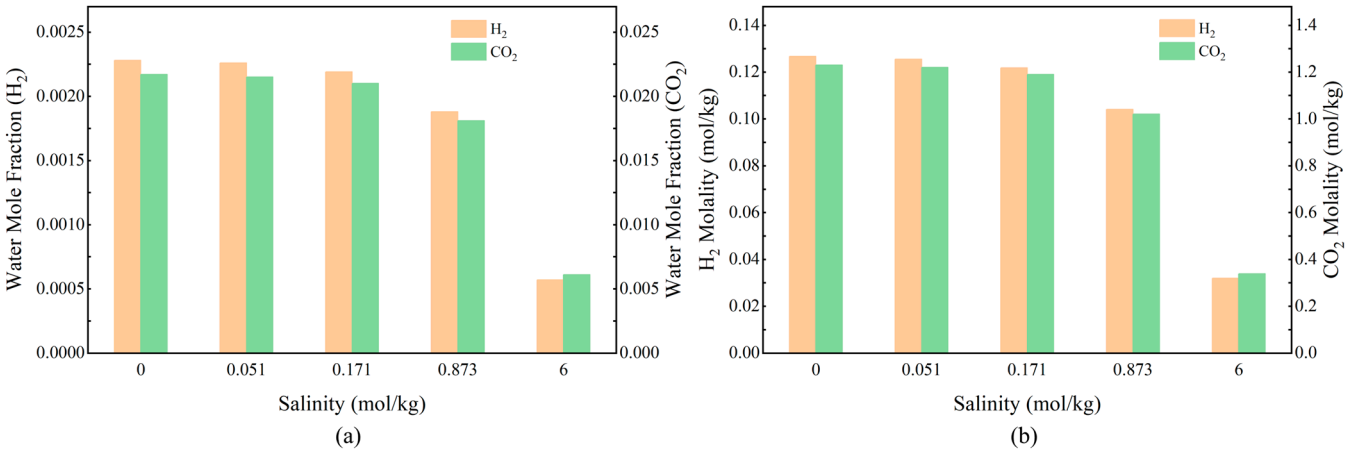


Figure 15. Dissolution changes of H_2 and CO_2 under different salinities: (**a**) The molar fraction of a gas in water, (**b**) The mass molar concentration of a gas.

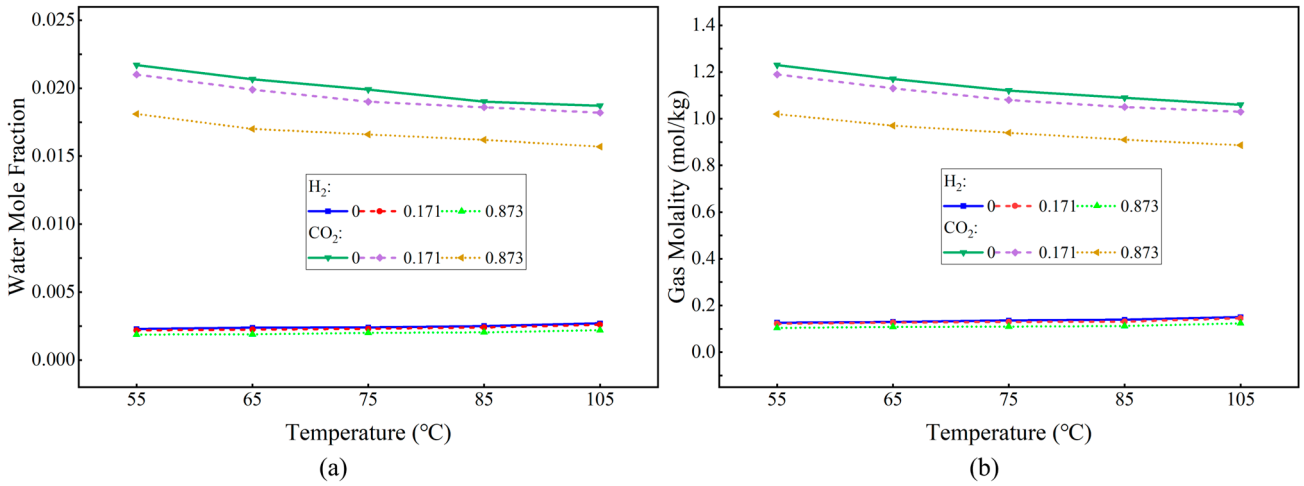


Figure 16. Dissolution variation in gas solubility with temperature under different salinities: (**a**) The molar fraction of a gas in water; (**b**) the mass molar concentration of a gas.

4.5. Effect of Capillary Pressure

Relative permeability hysteresis and capillary pressure jointly govern residual retention. In the fields of CCUS/CCS and UHS, there are numerous studies with and without capillary pressure [30,49,50]. Given that capillary pressure is governed by porosity and permeability, this study compares scenarios with and without capillary pressure under varying porosity–permeability conditions.

Figures 17 and 18 indicate that capillary pressure exerts the strongest control on residual gas distribution under low-porosity conditions. When porosity decreases to 0.05, residual gas becomes continuously accumulated over a large area due to enhanced capillary trapping in the narrowed pore throats. Under high porosity, the pore structure is more open and capillary effects weaken, leading to a substantially reduced difference in residual accumulation between the two conditions. CO_2 is more sensitive to these changes, whereas H_2—due to its low viscosity and high diffusivity—exhibits a smaller increase in residual saturation.

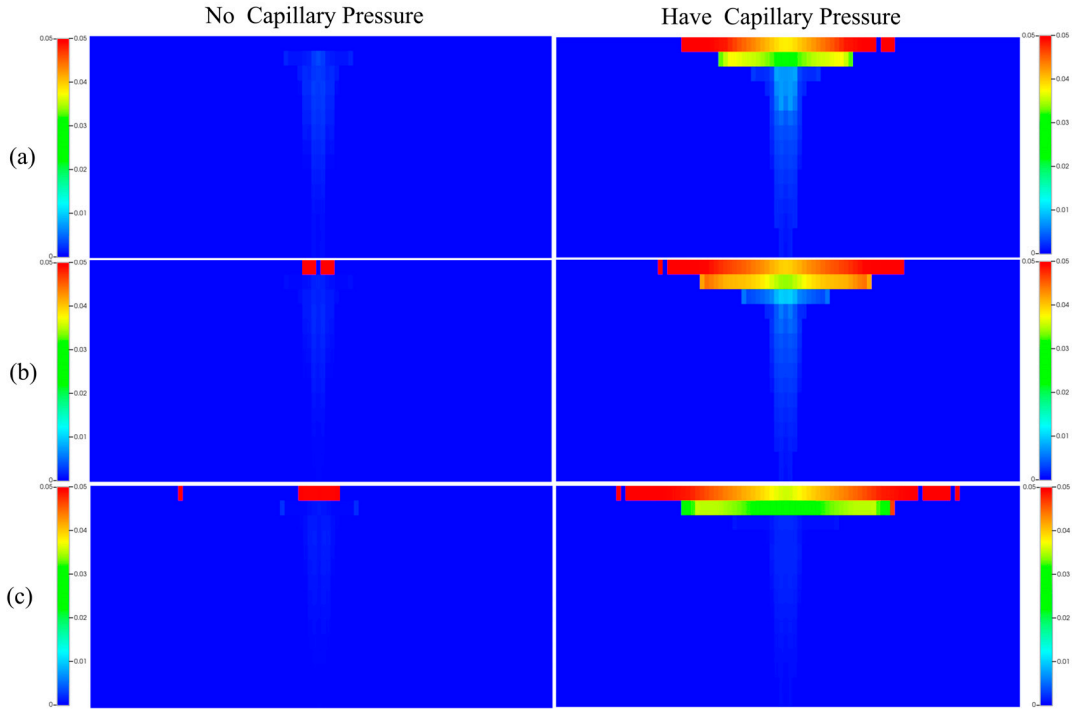


Figure 17. Residual saturation of H_2 at different porosities with and without the influence of capillary pressure: (**a**) 0.25, (**b**) 0.15, (**c**) 0.1.

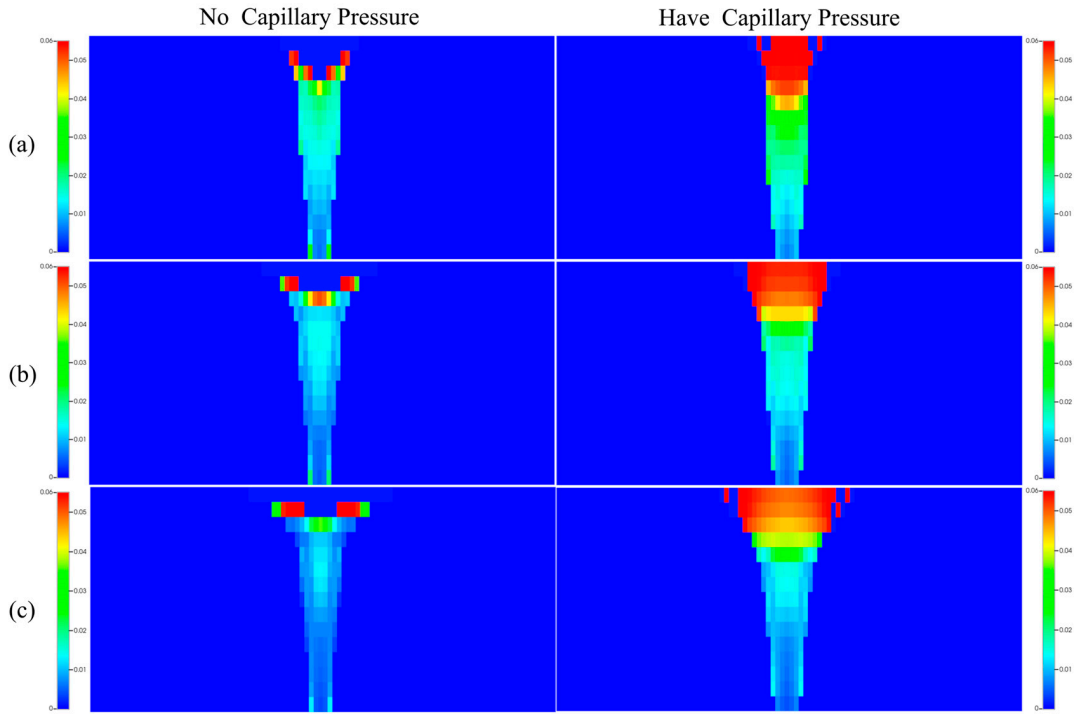


Figure 18. Residual saturation of CO_2 at different porosities with and without the influence of capillary pressure: (**a**) 0.25, (**b**) 0.15, (**c**) 0.1.

Figures 19 and 20 demonstrate that low K_v significantly amplifies the capillary trapping of H_2, while its influence on CO_2 residual retention remains comparatively modest. Under low K_v, the maximum residual saturation of H_2 increases by approximately 0.02, accompanied by a notable expansion of the residual accumulation zone. As K_v increases, pore-throat connectivity improves, enabling faster escape and reconnection of gas clusters, thereby reducing the capillary-dominated trapping of H_2.

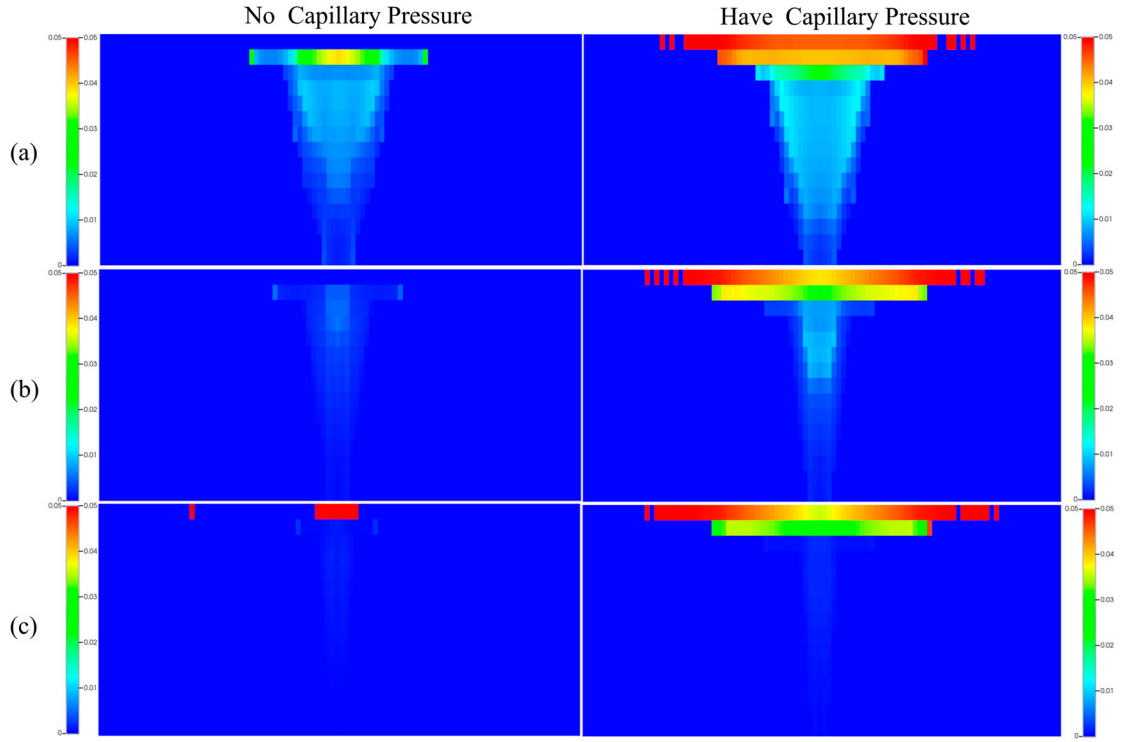


Figure 19. Residual saturation of H_2 at different K_v with and without capillary pressure: (**a**) 5 mD, (**b**) 15 mD, (**c**) 50 mD.

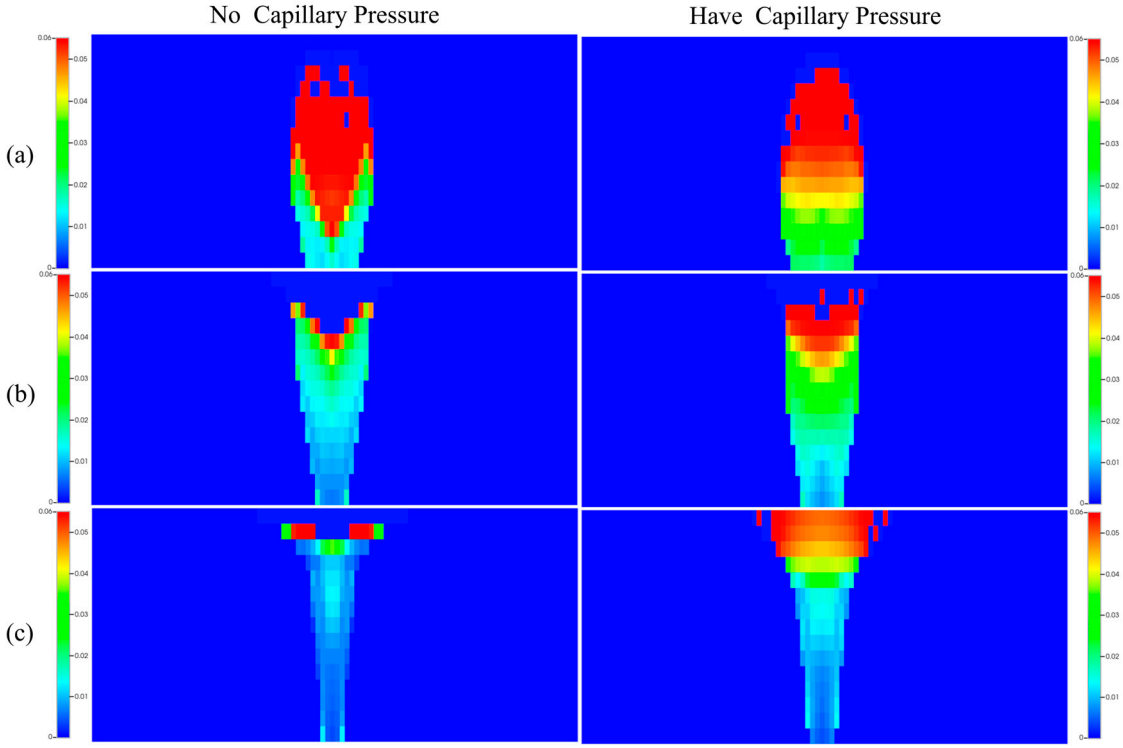


Figure 20. Residual saturation of CO_2 at different K_v without the influence of capillary pressure: (**a**) 5 mD, (**b**) 15 mD, (**c**) 50 mD.

Figures 21 and 22 show that under varying K_h, the capillary-pressure-controlled trapping behavior of the two gases is largely similar. At low K_h, weakened horizontal connectivity promotes the formation of high-saturation gas clusters, which become strongly immobilized by capillary forces, thus increasing residual saturation. As K_h increases,

capillary binding weakens, and the difference between simulations with and without capillary pressure becomes progressively smaller.

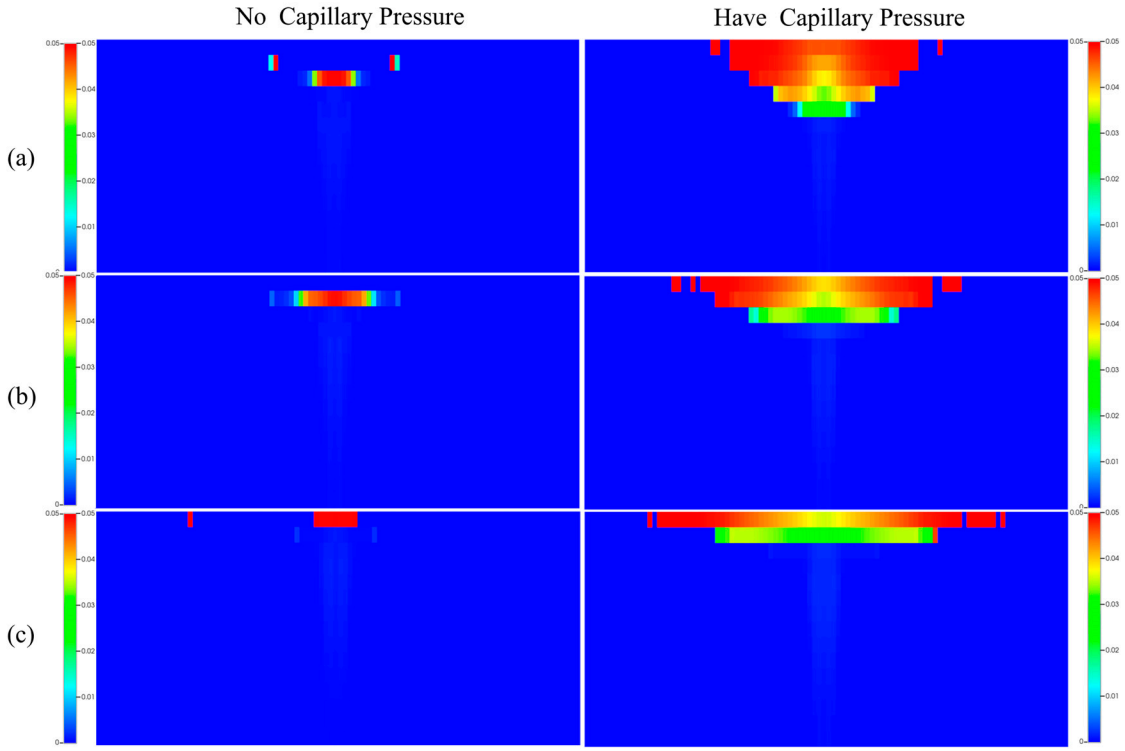


Figure 21. Residual saturation of H_2 at different K_h with and without the influence of capillary pressure: (**a**) 5 mD, (**b**) 15 mD, (**c**) 50 mD.

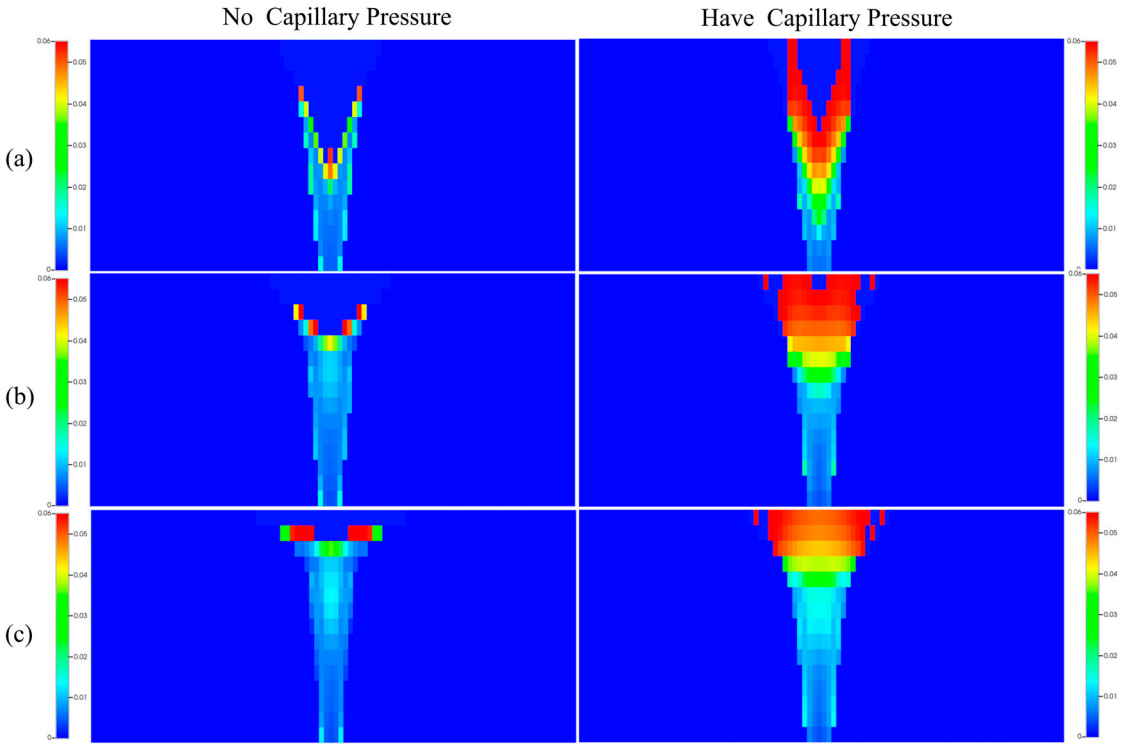


Figure 22. Residual saturation of CO_2 at different K_h with and without the influence of capillary pressure: (**a**) 5 mD, (**b**) 15 mD, (**c**) 50 mD.

5. Discussion

To investigate how multiple factors affect H_2 and CO_2 migration in saline aquifers, this paper constructs various 3D models in porosity, permeability, temperature, pressure, salinity, and capillary pressure. Further analysis is as follows:

(1) H_2 and CO_2 exhibit distinct migration behaviors. H_2 is characterized by low molecular weight, low viscosity, rapid migration, and low solubility. Its migration is primarily governed by physical transport, forming sharp gas tongues and extensive fingering. Its properties impose stringent requirements on caprock integrity. In contrast, CO_2 has a higher density and viscosity, exhibits flow dominated by viscous forces, resulting in limited migration. Its high solubility and strong residual favor storage stability. For H_2, lower solubility and residual reduce gas loss and help to enhance recovery.

(2) Reduced porosity narrows pore throats, increases tortuosity, and decreases flow cross-sectional area, thereby increasing flow resistance and promoting lateral spreading. Due to its low viscosity and high migration coefficient, H_2 is not very sensitive to changes in porosity, while the migration of CO_2 is more strongly affected because it depends on pressure-driven flow. Overall, high-porosity reservoirs reduce leakage risk.

(3) When K_v decreases, the vertical flow resistance increases, and the buoyancy drive of CO_2 in the vertical direction is suppressed, resulting in its formation of layered enrichment near the injection well. In contrast, due to H_2's strong buoyancy, it can partially overcome the resistance at low K_v and maintain a relatively high migration capacity. When K_h decreases, the horizontal conduction capacity weakens, the lateral expansion of gas is restricted, and the gas tends to form localized high-saturation zones. Due to the reduced horizontal displacement efficiency, gases tend to migrate along the vertical dominant path.

(4) Gas solubility is jointly controlled by temperature, pressure, and salinity. As pressure increases, the solubility of both gases rises because the increase in gas partial pressure exceeds that of Henry's constant. For CO_2, higher temperatures increase Henry's constant, reducing solubility. In contrast, H_2 exhibits a nonlinear temperature dependence of Henry's constant, peaking around 55 °C [51]. Above this, the constant decreases, enhancing solubility. Increasing salinity reduces available water for gas dissolution due to stable hydration structures, lowering solubility for both gases and weakening the temperature effect. It is noteworthy that, although high salinity significantly reduces gas solubility and increases the free-phase fraction of both H_2 and CO_2—thereby slightly expanding plume migration and enhancing caprock breach risk—the influence of salinity on the overall plume distribution is relatively minor. For both gases, the increase in free-phase gas primarily raises local gas saturation rather than altering the overall plume pattern. Despite H_2's higher diffusivity, its plume migration is more sensitive to salinity variations than that of CO_2. Nevertheless, compared with the influence of porosity and permeability, the expansion of H_2 plume migration induced by salinity remains very limited [42].

(5) Ignoring capillary pressure leads to a substantial underestimation of residual retention. However, although capillary pressure increases the overall level of residual trapping, it has only a minor influence on how residual retention varies with porosity and permeability. Its influence is mainly reflected in scale, and the changing trend is consistent. At low porosity, reduced pore size strengthens capillary forces, increasing residual gas saturation. This effect is stronger for CO_2 due to its lower interfacial tension, which promotes the formation of stable isolated gas clusters. In contrast, H_2 has higher interfacial tension, enabling easier reconnection and continued migration, resulting in weaker residual retention. Reductions in both K_v and K_h further enhance

capillary binding by restricting flow pathways and promoting locally elevated residual saturation. As capillary pressure is also essential for caprock sealing, future UHS studies should incorporate capillary effects more rigorously.

H_2 exhibits a significantly larger migration footprint than CO_2, which imposes stricter requirements on the regional sealing capacity and structural closure integrity of saline aquifers. In contrast, its migration behavior is less sensitive to variations in reservoir petrophysical properties (such as porosity and permeability), indicating that UHS site selection should prioritize large-scale structural traps and robust caprock sealing performance. Moreover, although H_2 solubility is more responsive than CO_2 to changes in reservoir conditions (pressure, temperature, and salinity), its absolute solubility remains very low, resulting in only limited practical variation. This further confirms the inherently low-loss characteristics of H_2 storage in saline aquifers. In contrast, for CCUS/CCS, emphasis is placed on storage mechanisms governed by dissolution and mineral reactions. In addition, this paper neglects molecular diffusion in its treatment of H_2 transport. However, the high diffusion of hydrogen may affect the long-term sealing performance. Recent work provides experimentally measured diffusion behavior [52]. This will provide support for subsequent inclusion in diffusion studies.

In this paper, the model adopts open boundaries in order to reflect the naturally unconfined lateral extent of many saline aquifers and to avoid the artificial pressure buildup that often occurs when closed boundaries are applied. All comparative cases are based on homogeneous models, and the use of a uniform cubic aquifer helps isolate the fundamental physical parameters that control the migration of H_2 and CO_2. In this way, any differences observed in plume behavior can be attributed directly to the specific parameters being examined.

However, real saline aquifers possess complex geological structures, and both reservoir properties and stratigraphic architectures are typically highly heterogeneous. Interactions among multiple factors may also lead to coupled effects that a homogeneous model cannot capture. Future research should therefore incorporate geological heterogeneity and investigate how different parameters jointly influence plume migration and trapping mechanisms.

6. Conclusions

This paper systematically investigates the effects of porosity, permeability, temperature, pressure, salinity, and capillary pressure on H_2 and CO_2 migration in saline aquifers. The conclusions are as follows:

(1) H_2 exhibits strong fingering and wide plume spread, with low solubility and weak residual retention, reducing storage losses. CO_2 shows compact, stable plumes with high solubility and strong residual retention, favoring long-term storage.

(2) Low porosity enhances lateral migration and residual retention, especially for CO_2. As porosity increases from 0.05 to 0.25, CO_2 plume expansion exceeds H_2 by over 50%, and the difference in maximum residual saturation rises from 16.7% to 77.8%.

(3) K_v significantly suppresses the upward migration of CO_2 and strengthens residual retention, whereas its effect on the H_2 migration range is less than 5%. Low K_h mainly restricts lateral spreading and only slightly increases residual retention, but the sensitivity of H_2 is lower than that of CO_2.

(4) The dissolution of H_2 and CO_2 is affected to different degrees by changes in the reservoir environment. Increased pressure promotes the dissolution of H_2 and CO_2. The increase in H_2 is approximately 16.15%, while CO_2 only rose by 7.49%. The temperature rise increases the solubility of H_2 and decreases that of CO_2. The increase in H_2 is approximately 15.56%, while the decrease in CO_2 is 13.82%. Increasing salinity

will simultaneously inhibit the dissolution of two gases, with the solubilities of H_2 and CO_2 decreasing by approximately 17.5% and 16.6%, respectively.

(5) High salinity weakens the temperature sensitivity of gas solubility. Compared with pure water, the solubility responses of H_2 and CO_2 to temperature in highly saline water decrease by about 1.06% and 0.6%, respectively.

(6) Ignoring capillary pressure underestimates residual retention. However, the capillary pressure is mainly reflected in an in increase in the retention scale and does not change the trend of residual retention controlled by different variables.

In this paper, the caprock sealing effect is simplified by imposing closed upper and lower boundaries. However, the actual breakthrough and leakage risks of caprocks, as well as biogeochemical reactions between injected gases and aquifer minerals or microorganisms, are not taken into consideration. Future work should adopt more realistic multi-field coupled models to investigate the complex, long-term migration processes of gases in saline aquifers.

Overall, this study provides a theoretical basis for applying the established conclusions of CCUS/CCS to UHS projects.

Author Contributions: Conceptualization, Z.S. and J.Q.; methodology, Z.S. and J.Q.; software, Z.S.; validation, Z.S.; formal analysis, Z.S.; investigation, Z.S., N.X., Y.Q., B.Z., L.C. and H.W.; resources, Z.S., N.X., Y.Q. and S.F.; data curation, Z.S.; writing—original draft preparation, Z.S.; writing—review and editing, Z.S., J.Q. and H.W.; visualization, Z.S. and H.W.; supervision, J.Q., N.X., Y.Q., B.Z., S.F. and L.C.; project administration, J.Q., N.X., B.Z. and S.F.; funding acquisition, N.X. All authors have read and agreed to the published version of the manuscript.

Funding: This research was funded by the National Key R&D Program of China, grant number 2023YFB4005500.

Data Availability Statement: The original contributions presented in this study are included in the article. Further inquiries can be directed to the corresponding authors.

Acknowledgments: The authors would like to thank the editor and the reviewers for their contributions.

Conflicts of Interest: The authors Liuping Chen and Hao Wang were employed by the company China National Salt Industry Group Co., Ltd. The remaining authors declare that the research was conducted in the absence of any commercial or financial relationships that could be construed as a potential conflict of interest.

Abbreviations

The following abbreviations are used in this manuscript:

UHS	Underground Hydrogen Storage
CCUS	Carbon Dioxide Capture, Utilization, and Storage
CCS	Carbon Dioxide Capture and Storage
PR–EOS	Peng–Robinson Equation Of State
CMG–GEM^{TM}	Computer Modeling Group Ltd.—General Equation of state Model
BHP	Bottom-Hole Pressure
K_v	Vertical Permeability
K_h	Horizontal Permeability

References

1. Sambo, C.; Dudun, A.; Samuel, S.A.; Esenenjor, P.; Muhammed, N.S.; Haq, B. A Review on Worldwide Underground Hydrogen Storage Operating and Potential Fields. *Int. J. Hydrogen Energy* **2022**, *47*, 22840–22880. [CrossRef]
2. Alms, K.; Ahrens, B.; Graf, M.; Nehler, M. Linking Geological and Infrastructural Requirements for Large-Scale Underground Hydrogen Storage in Germany. *Front. Energy Res.* **2023**, *11*, 1172003. [CrossRef]

3. Al-Shafi, M.; Massarweh, O.; Abushaikha, A.S.; Bicer, Y. A Review on Underground Gas Storage Systems: Natural Gas, Hydrogen and Carbon Sequestration. *Energy Rep.* **2023**, *9*, 6251–6266. [CrossRef]
4. Liu, N.; Wang, Y.; Bai, Q.; Liu, Y.; Wang, P.; Xue, S.; Yu, Q.; Li, Q. Road Life-Cycle Carbon Dioxide Emissions and Emission Reduction Technologies: A Review. *J. Traffic Transp. Eng. (Engl. Ed.)* **2022**, *9*, 532–555. [CrossRef]
5. Wang, W.; Wei, N.; Wei, F.; Ali, M.; Lin, K.; Lei, S. Research on the Progress of Carbon Capture, Utilization, and Storage (CCUS) Technologies Based on Bibliometric Analysis. *J. Clean. Prod.* **2025**, *529*, 146826. [CrossRef]
6. Thiyagarajan, S.R.; Emadi, H.; Hussain, A.; Patange, P.; Watson, M. A Comprehensive Review of the Mechanisms and Efficiency of Underground Hydrogen Storage. *J. Energy Storage* **2022**, *51*, 104490. [CrossRef]
7. Kang, N.; Sarsenbekuly, B.; Wu, H. Progress of CCUS Technology with Enhanced Oil Recovery. *J. CO_2 Util.* **2025**, *102*, 103233. [CrossRef]
8. Fratalocchi, L.; Rossini, S. A Review on the Role of Carbon Capture, Utilization and Storage (CCUS) in Energy Transition: An Industrial Perspective. *Appl. Catal. A Gen.* **2026**, *709*, 120660. [CrossRef]
9. Wang, C.; Wang, Z.; Li, H. Numerical Modelling of CO_2 Injection and Storage in Low Porosity and Low Permeability Saline Aquifers: A Design for the Permian Shiqianfeng Formation in the Yulin Area, Ordos Basin. *Sustainability* **2024**, *16*, 10593. [CrossRef]
10. Zuo, Q.; Zhang, Y.; Zhang, M.; Ju, B.; Ning, W.; Deng, X.; Yang, L.; Pang, C. Numerical Simulation of CO_2 Dissolution and Mineralization Storage Considering CO_2 -Water-Rock Reaction in Aquifers. *ACS Omega* **2024**, *9*, 45983–45995. [CrossRef]
11. Yang, D.X.; Zeng, R.S.; Zhang, Y.; Wang, Z.Q.; Wang, S.; Jin, C. Numerical Simulation of Multiphase Flows of CO_2 Storage in Saline Aquifers in Daqingzijing Oilfield, China. *Clean Techn Env. Policy* **2012**, *14*, 609–618. [CrossRef]
12. Zhao, M.; Wang, Y.; Gerritsma, M.; Hajibeygi, H. Efficient Simulation of CO_2 Migration Dynamics in Deep Saline Aquifers Using a Multi-Task Deep Learning Technique with Consistency. *Adv. Water Resour.* **2023**, *178*, 104494. [CrossRef]
13. Junji Yamaguchi, A.; Sato, T.; Tobase, T.; Wei, X.; Huang, L.; Zhang, J.; Bian, J.; Liu, T.-Y. Multiscale Numerical Simulation of CO_2 Hydrate Storage Using Machine Learning. *Fuel* **2023**, *334*, 126678. [CrossRef]
14. Xie, M.; Wang, S.; Feng, S.; Xu, C.; Li, X.; Sun, X.; Ma, Y.; Gan, Q.; Wang, T. A Stability Assessment of Fault-Caprock Trapping Systems for CO_2 Storage in Saline Aquifer Layers Using a Coupled THMC Model. *Energies* **2025**, *18*, 900. [CrossRef]
15. Chen, X.; Huang, Q.; Liu, P.; Du, J.; Guo, Y.; Xiong, Z. Numerical Simulation of CO_2 Sequestration Stability in Carbonate-Bearing Saline Aquifers: Effects of Mineral Dissolution. *Energy* **2025**, *335*, 138273. [CrossRef]
16. Pothana, P.; Ling, K.; Schultz, R.A. Rock Physics and Petrophysical Evaluation of Diagenetic Effects in the Broom Creek CO_2 Sequestration Site. *Geoenergy Sci. Eng.* **2026**, *257*, 214229. [CrossRef]
17. Bashir, A.; Ali, M.; Patil, S.; Aljawad, M.S.; Mahmoud, M.; Al-Shehri, D.; Hoteit, H.; Kamal, M.S. Comprehensive Review of CO_2 Geological Storage: Exploring Principles, Mechanisms, and Prospects. *Earth-Sci. Rev.* **2024**, *249*, 104672. [CrossRef]
18. Al Hameli, F.; Belhaj, H.; Al Dhuhoori, M. CO_2 Sequestration Overview in Geological Formations: Trapping Mechanisms Matrix Assessment. *Energies* **2022**, *15*, 7805. [CrossRef]
19. Chen, Y.; Wu, S.; Zhou, X.; Sun, T.; Chen, Q.; Liu, D.; Zhu, L.; Jia, S.; Wen, Z.; Xue, R. Sensitivity of Various Forms of CO_2 Sequestration to Different Parameters in Saline Aquifers in the Fushan Depression Based on Numerical Simulation. *Energy* **2025**, *319*, 135092. [CrossRef]
20. Ranganathan, P.; Van Hemert, P.; Rudolph, E.S.J.; Zitha, P.Z.J. Numerical Modeling of CO_2 Mineralisation during Storage in Deep Saline Aquifers. *Energy Procedia* **2011**, *4*, 4538–4545. [CrossRef]
21. Hamed, M.; Shirif, E. Sustainable CO_2 Storage Assessment in Saline Aquifers Using a Hybrid ANN and Numerical Simulation Model Across Different Trapping Mechanisms. *Sustainability* **2025**, *17*, 2904. [CrossRef]
22. Rezk, M.G.; Ibrahim, A.F. Impact of Rock Mineralogy on Reactive Transport of CO2 during Carbon Sequestration in a Saline Aquifer. *J. Petrol. Explor. Prod. Technol.* **2025**, *15*, 10. [CrossRef]
23. Fentaw, J.W.; Emadi, H.; Lloyd, H.; Ekwaro-Osire, S.; Okere, C.J.; Eyinla, D.S.; Kebir, A. Integrated Geochemical Modeling of Trapping Mechanisms and Sensitivity Analysis for Optimized CO_2 Sequestration in Saline Aquifers. *ACS Omega* **2025**, *10*, 53417–53437. [CrossRef] [PubMed]
24. Zivar, D.; Kumar, S.; Foroozesh, J. Underground Hydrogen Storage: A Comprehensive Review. *Int. J. Hydrogen Energy* **2021**, *46*, 23436–23462. [CrossRef]
25. Abdellatif, M.; Hashemi, M.; Azizmohammadi, S. Large-Scale Underground Hydrogen Storage: Integrated Modeling of Reservoir-Wellbore System. *Int. J. Hydrogen Energy* **2023**, *48*, 19160–19171. [CrossRef]
26. Jadhawar, P.; Saeed, M. Optimizing the Operational Efficiency of the Underground Hydrogen Storage Scheme in a Deep North Sea Aquifer through Compositional Simulations. *J. Energy Storage* **2023**, *73*, 108832. [CrossRef]
27. Zhao, Q.; Wang, Y.; Chen, C. Numerical Simulation of the Impact of Different Cushion Gases on Underground Hydrogen Storage in Aquifers Based on an Experimentally-Benchmarked Equation-of-State. *Int. J. Hydrogen Energy* **2024**, *50*, 495–511. [CrossRef]
28. Prigmore, S.; Okon-Akan, O.A.; Egharevba, I.P.; Ogbaga, C.C.; Okoye, P.U.; Epelle, E.; Okolie, J.A. Cushion Gas Consideration for Underground Hydrogen Storage. *Encyclopedia* **2024**, *4*, 847–863. [CrossRef]

29. Higgs, S.; Wang, Y.D.; Sun, C.; Ennis-King, J.; Jackson, S.J.; Armstrong, R.T.; Mostaghimi, P. Direct Measurement of Hydrogen Relative Permeability Hysteresis for Underground Hydrogen Storage. *Int. J. Hydrogen Energy* **2024**, *50*, 524–541. [CrossRef]
30. Zamehrian, M.; Gupta, I. Impact of Well Flow Dynamics and Formation Characteristics on Underground Hydrogen Storage in Aquifers. *Int. J. Hydrogen Energy* **2025**, *109*, 995–1007. [CrossRef]
31. Bai, F.; Jia, C.; Hu, J.; Alsousy, A.; Lu, Y.; Sepehrnoori, K. Storage Capacity Comparison of Hydrogen and Carbon Dioxide in Heterogeneous Aquifers. *Gas Sci. Eng.* **2024**, *121*, 205182. [CrossRef]
32. Harati, S.; Rezaei Gomari, S.; Gasanzade, F.; Bauer, S.; Pak, T.; Orr, C. Underground Hydrogen Storage to Balance Seasonal Variations in Energy Demand: Impact of Well Configuration on Storage Performance in Deep Saline Aquifers. *Int. J. Hydrogen Energy* **2023**, *48*, 26894–26910. [CrossRef]
33. Misaghi Bonabi, A.; Van Rooijen, W.; Al Kobaisi, M.; Vuik, C.; Hajibeygi, H. Comparative Analysis of Carbon Dioxide and Hydrogen Plume Migration in Aquifers Inspired by the FluidFlower Benchmark Study. *Int. J. Hydrogen Energy* **2025**, *135*, 56–68. [CrossRef]
34. Haynes, W.M. *CRC Handbook of Chemistry and Physics*; CRC Press: Boca Raton, FL, USA, 2016. [CrossRef]
35. Metz, B.; Davidson, O.; De Coninck, H.C.; Loos, M.; Meyer, L. *IPCC Special Report on Carbon Dioxide Capture and Storage*; Cambridge University Press: Cambridge, UK, 2005. [CrossRef]
36. Peng, D.-Y.; Robinson, D.B. A New Two-Constant Equation of State. *Ind. Eng. Chem. Fund.* **1976**, *15*, 59–64. [CrossRef]
37. Dalal Isfehani, Z.; Sheidaie, A.; Hosseini, M.; Fahimpour, J.; Iglauer, S.; Keshavarz, A. Interfacial Tensions of (Brine + H_2 + CO_2) Systems at Gas Geo-Storage Conditions. *J. Mol. Liq.* **2023**, *374*, 121279. [CrossRef]
38. Zhang, Y.; Tian, Y.; Sun, L.; Yuan, Z.; Wang, Y. Research and Application of Rock Fracturing Pressure Prediction Method for Deep Oil Reservoirs. *Sci. Rep.* **2025**, *15*, 10182. [CrossRef]
39. Corey, A.T.; Rathjens, C.H. Effect of Stratification on Relative Permeability. *J. Pet. Technol.* **1956**, *8*, 69–71. [CrossRef]
40. Land, C.S. Calculation of Imbibition Relative Permeability for Two- and Three-Phase Flow from Rock Properties. *Soc. Pet. Eng. J.* **1968**, *8*, 149–156. [CrossRef]
41. Krichevsky, I.R.; Kasarnovsky, J.S. Thermodynamical Calculations of Solubilities of Nitrogen and Hydrogen in Water at High Pressures. *J. Am. Chem. Soc.* **1935**, *57*, 2168–2171. [CrossRef]
42. Zhang, H.; Zhang, Y.; Arif, M. Impact of Formation Conditions and Well Configurations on Underground Hydrogen Storage. *Int. J. Hydrogen Energy* **2024**, *70*, 288–300. [CrossRef]
43. Carroll, J.J.; Mather, A.E. The System Carbon Dioxide-Water and the Krichevsky-Kasarnovsky Equation. *J. Solut. Chem.* **1992**, *21*, 607–621. [CrossRef]
44. Valderrama, J.O.; Campusano, R.A.; Forero, L.A. A New Generalized Henry-Setschenow Equation for Predicting the Solubility of Air Gases (Oxygen, Nitrogen and Argon) in Seawater and Saline Solutions. *J. Mol. Liq.* **2016**, *222*, 1218–1227. [CrossRef]
45. Ratnakar, R.R.; Venkatraman, A.; Kalra, A.; Dindoruk, B. On the Prediction of Gas Solubility in Brine Solutions with Single or Mixed Salts: Applications to Gas Injection and CO_2 Capture/Sequestration. *J. Nat. Gas Sci. Eng.* **2020**, *81*, 103450. [CrossRef]
46. Cai, Z.; Zhang, K.; Guo, C. Development of a Novel Simulator for Modelling Underground Hydrogen and Gas Mixture Storage. *Int. J. Hydrogen Energy* **2022**, *47*, 8929–8942. [CrossRef]
47. Al Homoud, R.; Barbosa Machado, M.V.; Daigle, H.; Sepehrnoori, K.; Ates, H. Enhancing Hydrogen Recovery from Saline Aquifers: Quantifying Wettability and Hysteresis Influence and Minimizing Losses with a Cushion Gas. *Hydrogen* **2024**, *5*, 327–351. [CrossRef]
48. Jia, Z.; Cao, R.; Pu, B.; Dehghanpour, H.; Cheng, L.; Zhang, Q.; Awotunde, A.A. Pore-Scale Binary Diffusion Behavior of Hydrogen-Cushion Gas in Saline Aquifers for Underground Hydrogen Storage: Optimization of Cushion Gas Type. *Fuel* **2025**, *381*, 133481. [CrossRef]
49. Bi, Z.; Guo, Y.; Yang, C.; Yang, H.; Wang, L.; He, Y.; Guo, W. Numerical Investigation of Fluid Dynamics in Aquifers for Seasonal Large-Scale Hydrogen Storage Using Compositional Simulations. *Renew. Energy* **2025**, *239*, 122101. [CrossRef]
50. Zhou, Y.; Tang, L.; Song, Z.; Pan, B.; Yue, M.; Liu, J.; Song, H. Research on CO2 Sequestration in Saline Aquifers with Different Relative Permeability Considering CO_2 Phase Conditions. *Energy* **2024**, *313*, 133739. [CrossRef]
51. Himmelblau, D.M. Solubilities of Inert Gases in Water. 0 °C to Near the Critical Point of Water. *J. Chem. Eng. Data* **1960**, *5*, 10–15. [CrossRef]
52. Banerjee, T.; Balasubramanian, G. Hydrogen Diffusion Induced Dislocation Transformations in a Nickel Superalloy. *Fuel* **2025**, *384*, 134064. [CrossRef]

Disclaimer/Publisher's Note: The statements, opinions and data contained in all publications are solely those of the individual author(s) and contributor(s) and not of MDPI and/or the editor(s). MDPI and/or the editor(s) disclaim responsibility for any injury to people or property resulting from any ideas, methods, instructions or products referred to in the content.